INTERNATIONAL JOURNAL FOR NUMERICAL METHODS IN FLUIDS
Int. J. Numer. Meth. Fluids 2008; **58**:57–89
Published online 17 January 2008 in Wiley InterScience (www.interscience.wiley.com). DOI: 10.1002/fld.1720

Buoyancy-corrected k–ε models and large eddy simulation applied to a large axisymmetric helium plume

W. Chung and C. B. Devaud*, †

Department of Mechanical and Mechatronics Engineering, University of Waterloo, 200 University Avenue West, Waterloo, Ont., Canada N2L3G1

SUMMARY

The present numerical study is focused on testing two different modeling approaches to simulate a large turbulent buoyant helium plume, in particular the near-field region. First, buoyancy-corrected k–ε models are applied in Reynolds-averaged Navier–Stokes (RANS) calculations, then large eddy simulation (LES) using a standard Smagorinsky model is examined. Good results are produced using the buoyancy-corrected models, in particular, excellent agreement is achieved for the radial profiles of the streamwise velocity. However, the predictions are very sensitive to the choice of the buoyancy constant, $C_{3\varepsilon}$, in the models. The present LES calculations show that the puffing frequency is accurately predicted. Predictions for the time-averaged velocities are within experimental uncertainty at all locations. The predicted plume concentrations are in good agreement at the base of the plume, but the centerline values are overpredicted farther downstream. The higher-order statistics are best predicted with the finest mesh. A sensitivity analysis on grid refinement, values of the Smagorinsky constant and the Schmidt number are included.

Received 13 September 2007; Revised 20 November 2007; Accepted 20 November 2007

KEY WORDS: buoyancy; models; helium; RANS; LES

1. INTRODUCTION

This study is focused on implementing and testing two different strategies to model the near-field region of a large axisymmetric turbulent buoyant helium plume. First, Reynolds-averaged Navier–Stokes (RANS) calculations will be examined using buoyancy-corrected k–ε models. Then, a large eddy simulation (LES) model will be investigated.

*Correspondence to: C. B. Devaud, Department of Mechanical and Mechatronics Engineering, University of Waterloo, 200 University Avenue West, Waterloo, Ont., Canada N2L3G1.
†E-mail: cdevaud@uwaterloo.ca

Contract/grant sponsor: NSERC

Buoyancy plays a key role in many physical processes such as the spread of smoke and toxic gases from fires, release of gases from exhaust stacks and volcanic eruptions. The far-field region of turbulent buoyant plumes has been investigated extensively and self-similarity functions for temperature and velocity profiles have been derived [1, 2]. For example, Shabbir and George [3] provided a comprehensive set of velocity and temperature measurements of a round thermal buoyant plume. The near-field flow dynamics including flow instability and laminar to turbulent flow transitions are not well understood. However, they were shown to be crucial in the flow development or fire growth in the context of fire and safety [1]. Toroidal vortices due to the Rayleigh–Taylor instability mode were observed in several experiments of helium–air plumes [4, 5]. The formation of these large vortices results in periodic oscillations called puffs. Cetegen and Ahmed [4] derived a correlation for the puffing frequency as a function of the Richardson number. Other studies compared non-reacting buoyant flows with diffusion flames and related the puffing frequency to different parameters such as ambient pressure, exit velocity and type of co-flowing oxidizer [6, 7].

There are significant benefits in developing reliable numerical methods and turbulence models applied to non-reacting buoyant plumes. A large-scale helium–air plume gives a realistic representation of the generation of turbulence from buoyancy without the complexities of combustion and radiation that would take place in a fire. Furthermore, it is crucial to develop and validate computational tools in close conjunction with experimental techniques in order to have a full set of tools available to study fluid flow and heat transfer in large-scale situations. A simulation run using a well-validated computational fluid dynamics (CFD) code can provide accurate information at any time and any point in space. Equivalent information may be difficult to retrieve from an experimental investigation.

Within the present framework of investigating a large buoyant plume, direct numerical simulations remain out of reach due to the wide range of length and time scales that need to be fully resolved. Instead, CFD techniques based on RANS and LES are considered. RANS calculations are based on ensemble-averaged flow equations where the unclosed Reynolds stress tensor may be approximated using a two-equation eddy viscosity model such as k–ε or a Reynolds stress formulation.

Different levels of success were achieved with buoyancy-modified RANS models. Previous numerical studies [8, 9] used buoyancy corrections applied to the k–ε model and the algebraic stress model (ASM) and obtained comparable results for both approaches. Chow and Mok [10] tested four turbulence models, ASM, k–ε, low Reynolds number k–ε and a hybrid version between k–ε and ASM for compartment pool fires. Evaluation of the four approaches resulted in similar predictions with CPU time between 6.3 and 29.5% greater than that required for the k–ε model. Thus, the latter has remained the model of choice due to lack of significant benefits from other RANS models. Markatos and Malin [11] modeled buoyancy-induced smoke flow in a two-dimensional enclosure using a k–ε model. They found that the addition of the source term did improve the realism of the predictions. The correct trends were captured when compared with the experimental data, but the model results did tend to overpredict the depth of the hot layer within the enclosure.

Two common modeling expressions are used to determine the buoyancy production in the turbulent kinetic energy: one using the simple gradient diffusion hypothesis (SGDH) and the other based on the generalized gradient diffusion hypothesis (GGDH) [12]. Previous work [13–16] showed that the SGDH brought no or little improvement in the velocity and temperature predictions compared with the k–ε model without any buoyancy source term. Nam and Bill [13] successfully corrected the SGDH deficiency for fire plumes by adjusting C_μ and the turbulent Prandtl number σ_t.

DOI: 10.1002/fld

Best agreement with experimental data was usually obtained with the GGDH approach [14, 15]. Recently, Van Maele and Merci [16] examined the k–ε and the realizable k–ε models combined with the SGDH and GGDH closure for two different buoyant plumes and concluded that both performed well with the GGDH closure. However, Brescianini and Delichatsios [17] undertook a comparative study on newer experiments and concluded that the most suitable buoyancy model was dependent on the set of experimental data. For clarity, a summary of the buoyancy modifications for the numerical models mentioned above is listed in Tables I and II.

In LES, the large turbulent flow structures containing most of the energy are resolved explicitly, while the dissipation scales are modeled. Consequently, the instantaneous resolved flowfield can be provided with greater accuracy, whereas most of this information is lost in RANS. Thus, the transient nature of turbulent buoyant plumes may be captured and more flow details can be provided. Very few LES results have been reported for the near field of buoyant plumes. Zhou *et al.* [20] performed a detailed LES study on several buoyant heated plumes and reproduced many characteristics of buoyant plumes such as the energy decay and the velocity profiles. Desjardin *et al.* [21] used LES including dynamic Smagorinsky subgrid scale model for the large axisymmetric helium plume, experimentally studied by O'Hern *et al.* [22]. Their results showed some success in predicting trends but pointed out a large variability on the Smagorinsky constant and grid resolution.

In this study, detailed comparison of the computational results with well-documented experimental data [22] will be shown. Several buoyancy-corrected k–ε models will be revisited in the context of reproducing the near-field flow dynamics. The first objective is to evaluate the strengths and weaknesses of these RANS models in the near field of a large turbulent buoyant plume.

Table I. Summary of buoyancy modifications for the source term in ε equation that excludes the flux Richardson number.

Reference	R_f	$C_{3\varepsilon}$	G
Davidson [8]	—	1.44	$-\frac{\mu_t}{\sigma_t}\frac{1}{\overline{\rho}}\frac{\partial\overline{\rho}}{\partial x_j}g_j$
Shabbir and Taulbee [9]	—	1.44	$-\frac{\mu_t}{\sigma_t}\frac{1}{\overline{\rho}}\frac{\partial\overline{\rho}}{\partial x_j}g_j$
Chow and Mok [10]	—	1.44	$-\frac{3}{2}\frac{\mu_t}{\sigma_t\overline{\rho}k}\overline{u'_j u'_k}\frac{\partial\overline{\rho}}{\partial x_k}g_j$
Annarumma *et al.* [18]	—	1.44	$-\frac{\mu_t}{\sigma_t}\frac{1}{\overline{\rho}^2}\frac{\partial\overline{\rho}}{\partial x_j}\left(\frac{\partial\overline{p}}{\partial x_j}+\rho_\infty g_j\right)$
Nam and Bill [13]	—	1.44	$-\mu_t\frac{1}{\overline{\rho}}\frac{\partial\overline{\rho}}{\partial x_j}g_j$
Brescianini and Delichatsios [17]	—	1.0	$-\frac{\mu_t}{\sigma_t}\frac{1}{\overline{\rho}^2}\frac{\partial\overline{\rho}}{\partial x_j}\left(\frac{\partial\overline{p}}{\partial x_j}+\rho_\infty g_j\right)$ $-\frac{3}{2}\frac{\mu_t}{\sigma_t\overline{\rho}^2 k}\left(\overline{u'_j u'_k}\frac{\partial\overline{\rho}}{\partial x_k}\right)\left(\frac{\partial\overline{p}}{\partial x_j}+\rho_\infty g_j\right)$

$S_\varepsilon = C_{1\varepsilon}\frac{\varepsilon}{k}P + C_{3\varepsilon}\frac{\varepsilon}{k}G - C_{2\varepsilon}\overline{\rho}\frac{\varepsilon^2}{k}$.

DOI: 10.1002/fld

Table II. Summary of buoyancy modifications for the source term in ε equation that includes the flux Richardson number.

Reference	R_f	$C_{3\varepsilon}$	G
Markatos and Malin [11]	$-\frac{G}{P+G}$	0.9	$-\frac{\mu_t}{\sigma_t}\frac{1}{\overline{\rho}}\frac{\partial\overline{\rho}}{\partial x_j}g_j$
Xue *et al.* [19]	Not specified	0.8	$-\frac{\mu_t}{\sigma_t}\frac{1}{\overline{\rho}}\frac{\partial\overline{\rho}}{\partial x_j}g_j$
Yan and Holmstedt [14]	Not specified	0.6	$-\frac{3}{2}\frac{\mu_t}{\sigma_t\overline{\rho}k}\overline{u'_ju'_k}\frac{\partial\overline{\rho}}{\partial x_k}g_j$
Worthy *et al.* [15]	$-\frac{G}{P+G}$	Varied	$-\frac{\mu_t}{\sigma_t}\frac{1}{\overline{\rho}}\frac{\partial\overline{\rho}}{\partial x_j}g_j$ $-\frac{3}{2}\frac{\mu_t}{\sigma_t\overline{\rho}k}\overline{u'_ju'_k}\frac{\partial\overline{\rho}}{\partial x_k}g_j$
Van Maele and Merci [16]	$-\frac{G}{P+G}$	0.8	$-\frac{\mu_t}{\sigma_t}\frac{1}{\overline{\rho}^2}\frac{\partial\overline{\rho}}{\partial x_j}\left(\frac{\partial\overline{p}}{\partial x_j}+\rho_\infty g_j\right)$ $-\frac{3}{2}\frac{\mu_t}{\sigma_t\overline{\rho}^2k}\left(\overline{u'_ju'_k}\frac{\partial\overline{\rho}}{\partial x_k}\right)\left(\frac{\partial\overline{p}}{\partial x_j}+\rho_\infty g_j\right)$

$S_\varepsilon = C_{1\varepsilon}\frac{\varepsilon}{k}(P+G)(1+C_{3\varepsilon}R_f) - C_{2\varepsilon}\overline{\rho}\frac{\varepsilon^2}{k}$.

The second objective is to perform a detailed investigation of three-dimensional and transient LES using a standard Smagorinsky approach in order to further assess potential benefits and additional costs compared with RANS calculations.

2. TURBULENCE MODELS

In this section, two different turbulence modeling strategies are examined in order to include the buoyancy effect: one relies on the k–ε model and the second approach is based on LES.

2.1. Buoyancy-corrected k–ε models

The standard k–ε model [23] is based on the eddy viscosity concept where the Reynolds stress components are determined as follows:

$$-\overline{\rho}\widetilde{u''_iu''_j} = 2\mu_t\widetilde{S_{ij}} - \tfrac{2}{3}\overline{\rho}k\delta_{ij} \tag{1}$$

where $\overline{\rho}$ is the mean density, μ_t the turbulent viscosity, $\widetilde{S_{ij}}$ is the Favre-average strain tensor and k the turbulent kinetic energy. The turbulent viscosity is calculated using

$$\mu_t = \overline{\rho}C_\mu\frac{k^2}{\varepsilon} \tag{2}$$

DOI: 10.1002/fld

C_μ being a constant equal to 0.09 and ε is the turbulent dissipation rate. The steady transport equations for k and ε are given by

$$\frac{\partial}{\partial x_j}(\overline{\rho}\tilde{u_j}k)=\frac{\partial}{\partial x_j}\left[\left(\mu+\frac{\mu_t}{\sigma_k}\right)\frac{\partial k}{\partial x_j}\right]+P+G-\overline{\rho}\varepsilon \tag{3}$$

$$\frac{\partial}{\partial x_j}(\overline{\rho}\tilde{u_j}\varepsilon)=\frac{\partial}{\partial x_j}\left[\left(\mu+\frac{\mu_t}{\sigma_\varepsilon}\right)\frac{\partial \varepsilon}{\partial x_j}\right]+C_{1\varepsilon}\frac{\varepsilon}{k}P-C_{2\varepsilon}\overline{\rho}\frac{\varepsilon^2}{k}+S_{\varepsilon\mathrm{B}} \tag{4}$$

where $\tilde{u_j}$ is the Favre-average velocity, μ is the molecular viscosity and P is the production of turbulence due to shear:

$$P=-\overline{\rho}\widetilde{u_i''u_j''}\left(\frac{\partial \tilde{u_i}}{\partial x_j}\right) \tag{5}$$

G is the production of turbulence due to buoyancy. Standard values are used for the following constants: $C_{1\varepsilon}=1.44, C_{2\varepsilon}=1.92, \sigma_k=1.0$ and $\sigma_\varepsilon=1.3$ [23]. The production of turbulence due to buoyancy is commonly modeled with the SGDH approach, namely,

$$G=-\frac{\mu_t}{\sigma_t}\frac{1}{\overline{\rho}^2}\frac{\partial \overline{\rho}}{\partial x_j}\left(\frac{\partial \overline{p}}{\partial x_j}+\rho_\infty g_j\right) \tag{6}$$

where $\overline{p}$ is the mean pressure, σ_t is the turbulent Prandtl number set to 0.85, ρ_∞ is the reference density corresponding to the density of air in the free stream and g is the gravity. The standard k–ε model has been widely used due to its simplicity, robustness and well-documented validation tests. However, the formulation based on SGDH results in well-known deficiencies such as the underprediction of the spreading rate of vertical thermal plumes and the overprediction of the spreading rate of horizontal stratified flows [13, 18].

To overcome the underprediction of the buoyancy source term G, in Equation (3), an alternative expression based on the GGDH given by Daly and Harlow [12] can be used:

$$G=-\frac{3}{2}\frac{\mu_t}{\sigma_t\overline{\rho}^2k}\left(\overline{u_j'u_k'}\frac{\partial \overline{\rho}}{\partial x_k}\right)\left(\frac{\partial \overline{p}}{\partial x_j}+\rho_\infty g_j\right) \tag{7}$$

The primary difference between the SGDH (Equation (6)) and GGDH (Equation (7)) models is the inclusion of the cross-stream density variation, $\partial\overline{\rho}/\partial x_k$, in GGDH, whereas the SGDH model includes only the streamwise density gradient for the vertical plume. It should be noted that the normal stresses $\widetilde{u_k''u_k''}$ (no summation here) in the main flow direction are approximated as being equal to the turbulent kinetic energy k. This is justified by the fact that the k–ε model does not predict the normal stresses very well and that these are twice the magnitude of the components of the normal stress tensor in the other two directions, as shown in the experiments [22].

Further correction may be applied to the transport equation of ε where one additional source, $S_{\varepsilon\mathrm{B}}$, is added, as shown in Equation (4). Various expressions can be found for $S_{\varepsilon\mathrm{B}}$ depending on the orientation of the plume (horizontal or vertical layers) and the definition of the flux Richardson term used [10, 15, 19, 24]. The flux Richardson number is the ratio of the rate of removal of energy by buoyancy to its production by the shear and is expressed as, $R_\mathrm{f}=-G/P$. An alternative definition and one that is now taken as the standard is given by Rodi as $R_\mathrm{f}=-G/(P+G)$ [25].

DOI: 10.1002/fld

A detailed comparison of the expressions for $S_{\varepsilon B}$ can be found in Van Maele and Merci [16]. In this study, the model used by Van Maele and Merci [16] and Markatos and Malin [11] is selected:

$$S_{\varepsilon B} = C_{1\varepsilon}(1 - C_{3\varepsilon})\frac{\varepsilon}{k}G \tag{8}$$

where $C_{3\varepsilon}$ is the buoyancy constant. Past simulations of thermal plumes [11, 13, 14] and isothermal helium plume [16] indicated that the results were insensitive to the value of $C_{3\varepsilon}$ between 0.3 and 1.0. A sensitivity analysis will be performed by varying $C_{3\varepsilon}$ from 0 to 1 in Section 5.1.1. For comparison, the expression used in the commercial CFD package Ansys CFX [26] is shown:

$$S_{\varepsilon B} = C_{1\varepsilon}C_3\frac{\varepsilon}{k}\max(0, G) \tag{9}$$

$$G = -\frac{\mu_t}{\rho\sigma_\rho}\frac{\partial\overline{\rho}}{\partial x_j}g_j \tag{10}$$

where C_3 is a constant set to a default value of unity. Equation (10) is based on the SGDH expression (Equation (6)) where the pressure gradient is neglected and ρ_∞ is assumed to be equal to the mean density $\overline{\rho}$. Further, the default CFX buoyancy-corrected k–ε model corresponds to Equation (8) with $C_{3\varepsilon} = 0$.

2.2. LES

The LES code used in this study is the fire dynamics simulator (FDS) made available through the National Institute of Standards and Technology. FDS solves the low-Mach number form of the compressible Navier–Stokes equations. The filtering process in LES introduces unclosed quantities that are not resolved, such as the subgrid Reynolds stress, the subgrid heat and mass flux, the combustion heat release rate and the radiation loss. In this study, the flow under consideration is isothermal. Thus, the approximations related to combustion and heat transfer are not discussed. FDS has been previously used with success for a variety of reacting and non-reacting flows [27, 28]. The subgrid Reynolds stress, τ_{ij}, is modeled using a standard Smagorinsky model [29] where the subgrid scale eddy viscosity is calculated by

$$\mu_{\text{sgs}} = \rho C_{\text{s}}^2\Delta^2|S| \tag{11}$$

where ρ is the density, C_{s} the Smagorinsky constant, $|S|$ the filtered rate of strain and Δ the filter width defined as $(\Delta_x\ \Delta_y\ \Delta_z)^{1/3}$, where Δ_x, Δ_y and Δ_z correspond to the grid spacing in the x, y and z directions, respectively. In the present calculations, C_{s} is set to 0.2 but sensitivity of the results to C_{s} will be examined.

The subgrid diffusivity, D_{sgs}, is determined by

$$D_{\text{sgs}} = \frac{1}{\rho}\frac{\mu_{\text{sgs}}}{Sc} \tag{12}$$

Sc being the subgrid Schmidt number is equal to 0.5. Different values of Sc will be tested.

The baroclinic torque due to the non-alignment of the density and pressure gradients is included in the momentum equation.

DOI: 10.1002/fld

3. CASE STUDY: THE AXISYMMETRIC HELIUM PLUME

The axisymmetric buoyant plume selected for this study corresponds to the experiments performed by O'Hern *et al.* [22] at Sandia National Laboratories in Albuquerque, New Mexico. In this section, the experimental conditions are briefly summarized. As shown in Figure 1(a) and (b), the experimental setup consists of a cubical enclosure of 6.1 m length with a 2.3 m diameter chimney located on top of the chamber. Air enters the domain through an annular air duct and the flow is

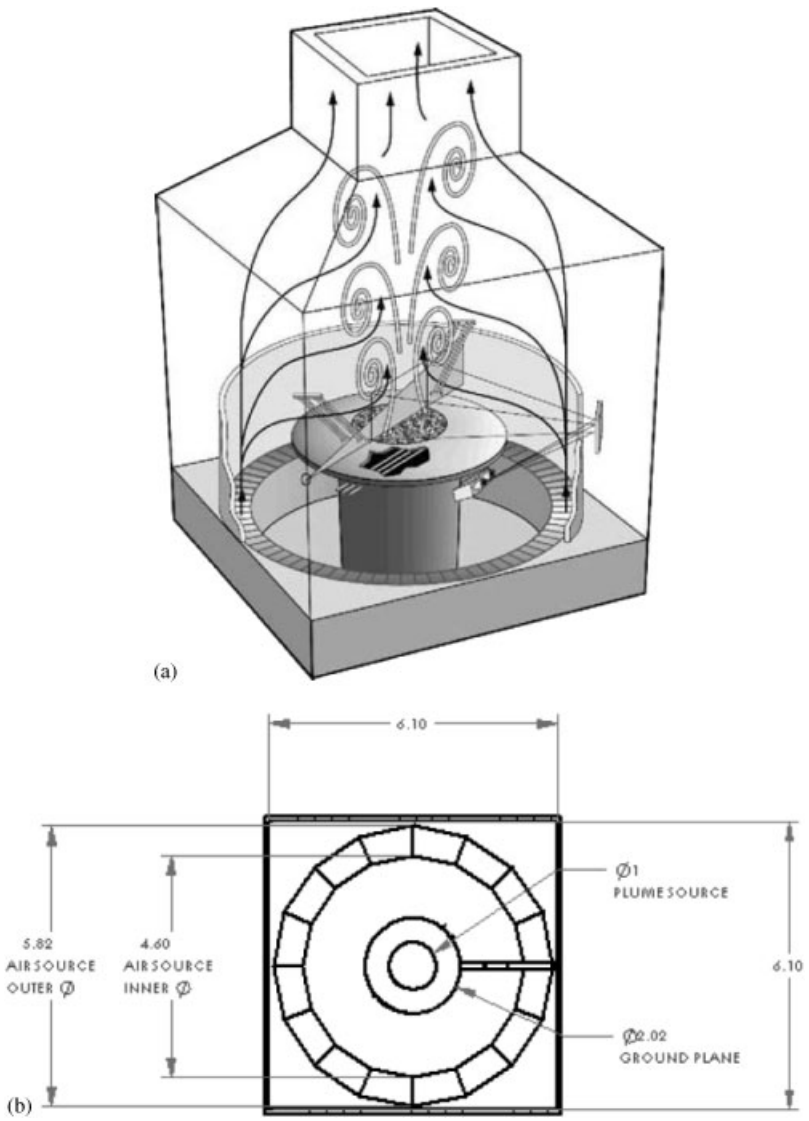

Figure 1. Experimental setup from O'Hern *et al.* [22]: (a) schematic and (b) horizontal view with dimensions in m.

DOI: 10.1002/fld

straightened through a honeycomb apparatus to help maintain flow uniformity. The helium plume enters the chamber through a 1 m diameter opening located 1.74 m above the air duct. This is surrounded by a 0.51 m platform to simulate the 'ground plane' and causes the surrounding air to be drawn in radially. In the experiment, acetone is introduced into the helium flow to be used as the fluorescent tracer gas at 1.7 vol%. Oxygen is also added to the helium mixture at 1.9 vol% to quench the acetone phosphorescence. This results in a plume molecular weight of 5.45 g/mol. Air enters the chamber at an average normal velocity of 0.15 m/s and the helium plume enters the chamber at an average normal velocity of 0.325 m/s. The average mixture Reynolds number, Re, is equal to 3200. Data were gathered after initial transients had passed through the chamber and the experiment had reached a quasi-steady state. Experimental data are available in the near-field region (i.e. up to 0.9 m above the plume source) for the cross-stream and streamwise velocity, plume concentration, root mean square (rms) of the velocities, rms of the plume concentration, turbulent kinetic energy and the cross-correlation between the fluctuations of the streamwise velocity and plume concentration [30]. The experimental uncertainty on the measured velocities, concentrations, the turbulent statistics and concentration fluctuations is estimated to be around ± 20, ± 18, ± 30 and $\pm 21\%$, respectively [30].

4. NUMERICAL DETAILS

4.1. Implementation in a RANS code

The buoyancy-corrected k–ε transport equations (Equations (3) and (4)) are implemented within the commercial CFD package, CFX [26]. The SGDH model (Equation (6)) and the GGDH expression (Equation(7)) for G, as well as the additional source term $S_{\varepsilon \mathrm{B}}$ (Equation (8)), are included using CFX expression language functions based on FORTRAN subroutines. CFX features a coupled implicit solver for the governing equations (conservations of mass, momentum and scalar quantities). Advection is discretized using a second-order scheme and a second-order central differencing scheme is applied to diffusion. Simulations are run until all maximum residuals for the momentum, turbulence and species equations were less than 10^{-4}. A lower convergence criterion equal to 10^{-5} did not produce any significant differences in the predicted velocity and plume concentration.

As shown in Figure 2(a), a slice of the axisymmetric domain is considered due to symmetry. Calculations using the full three-dimensional domain were also performed and the differences in the results between the two computational domains were found to be negligible. The smaller computational domain is kept due to lower run times. The mesh consists of 22 882 unevenly spaced hexahedral cells and is one node thick in the circumferential direction. The plume inlet, platform surrounding the plume inlet as well as the air inlet are all defined according to the experimental setup. Mesh dependency tests showed that the predicted velocities and plume concentrations were grid independent. No slip condition is applied to the wall boundaries. A 5% turbulence intensity is set at all inlet boundary conditions. Varying the turbulence intensity between 1 and 5% produced negligible effect in the results. Static pressure opening boundaries are defined for the side walls and the roof. The plume gas composition consists of helium, acetone and oxygen at concentrations of 0.71, 0.18 and 0.11 in mass, respectively. The plume gas enters the domain at the plume inlet with a uniform normal velocity profile equal to 0.325 m/s. The air inlet velocity profile is uniform at 0.15 m/s. A constant temperature of 284 K and atmospheric pressure were assumed.

DOI: 10.1002/fld

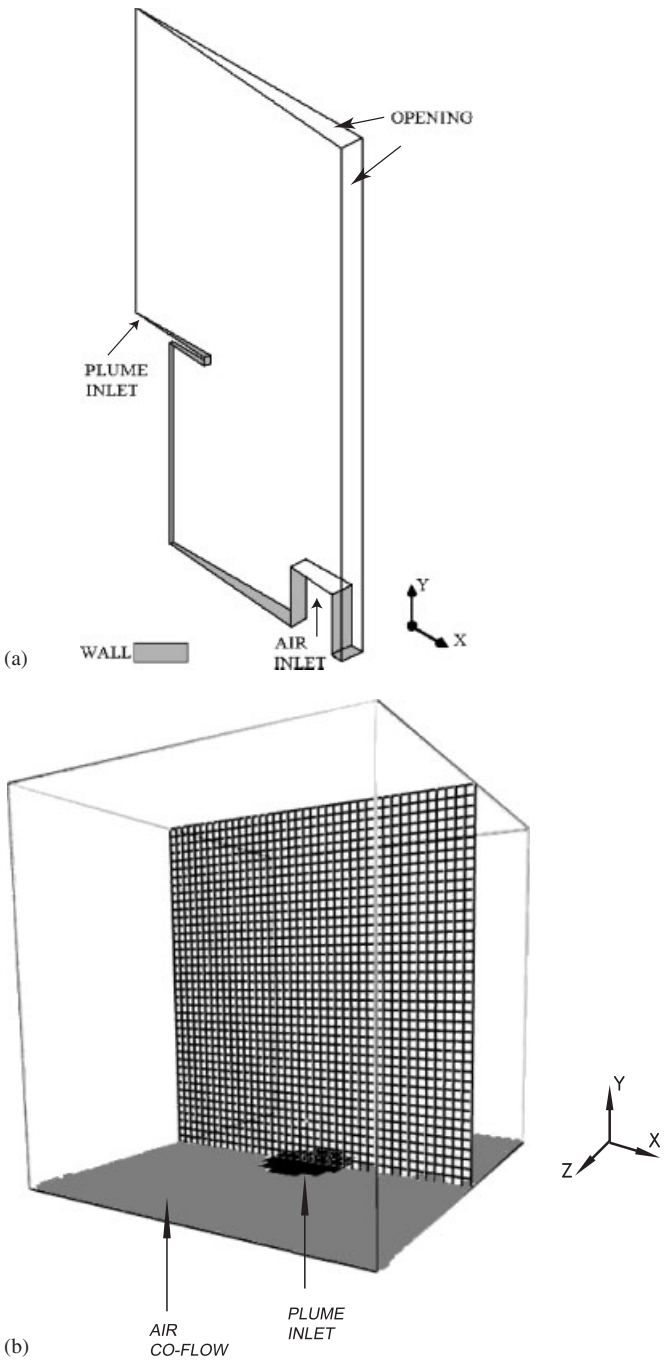

Figure 2. Computational domains: (a) RANS and (b) LES.

DOI: 10.1002/fld

The simulations were run on one Pentium IV processor and the CPU time was approximately 2.5 h.

4.2. Three-dimensional LES

The governing equations are advanced in time using a second-order MacCormak scheme. Spatial derivatives are estimated with second-order accurate finite differences on a rectangular grid, with scalar quantities assigned to the center of grid cells and velocity quantities assigned to cell faces. Convective terms are upwind biased, based on a Courant–Friedrichs–Lewy condition, in the predictor step and downwind biased in the corrector step. Diffusive terms are central differenced. The Poisson equation is solved using a direct fast-Fourier-transform-based solver.

As seen in Figure 2(b), the experimental setup is simplified into a 4 m cubic enclosure for the present LES. The plume inlet is located at the center of the bottom plane and a surrounding air-coflow is also defined. Only structured rectangular grids are allowed in FDS. Thus, the plume inlet is adjusted using a stair-stepped approximation of the circular geometry and keeping the area as close as possible to the experimental dimensions. The inlet plume velocity is corrected to ensure that the plume inlet mass flow rate is consistent with that of the experiment. Values for the area and velocity for the four grid sizes used are displayed in Table III. This adjustment is also applied to the air inflow rate. The experimental mixture of helium, acetone and oxygen is approximated as a single gas with the same molecular weight of 5.45 g/mol. The remaining surfaces are modeled as openings. A uniform mesh is used, i.e. $\Delta_x = \Delta_y = \Delta_z = \Delta$ in order to avoid any problem of permutation for the Fourier transforms in FDS. Four grid sizes are tested and expressed in terms of plume diameter to grid cell size ratio, $\Delta/D = 10, 20, 40$ and 80, resulting in $64 \times 10^3, 512 \times 10^3, 4096 \times 10^3$ and $32\,768 \times 10^3$ cells, respectively. The initial condition is quiescent air at 284 K and 1 atm. FDS adds random vorticity perturbations to the initial velocity field. Calculations using the first three grids were run on one single Xeon processor. The simulations with the finest mesh required 16 Xeon processors and message passing interface was used.

The LES calculations are set up to gather data every 0.05 s of physical time at most. The first 10 s allows for the initial computational flow transients to move downstream and to reach quasi-steady flow conditions. Results from the second 10 s of simulation are compiled to produce the time-averaged quantities. The values were compared with those of varying time intervals to ensure that the initial flow transients were excluded and a sufficient time interval was used to obtain the time-averaged statistics. Table III shows the CPU time needed for the simulations with the four grids.

Table III. Plume inlet area, velocity and CPU time for the grid sizes used in LES.

	Grid spacing (m)	Area (m^2)	Velocity (m/s)	CPU time (h)
Grid I	0.100	0.800	0.319	0.11
Grid II	0.050	0.790	0.323	1.99
Grid III	0.025	0.790	0.323	31.77
Grid IV	0.0125	0.785	0.325	50.32
Experiments [22]	N/A	0.785	0.325	N/A

DOI: 10.1002/fld

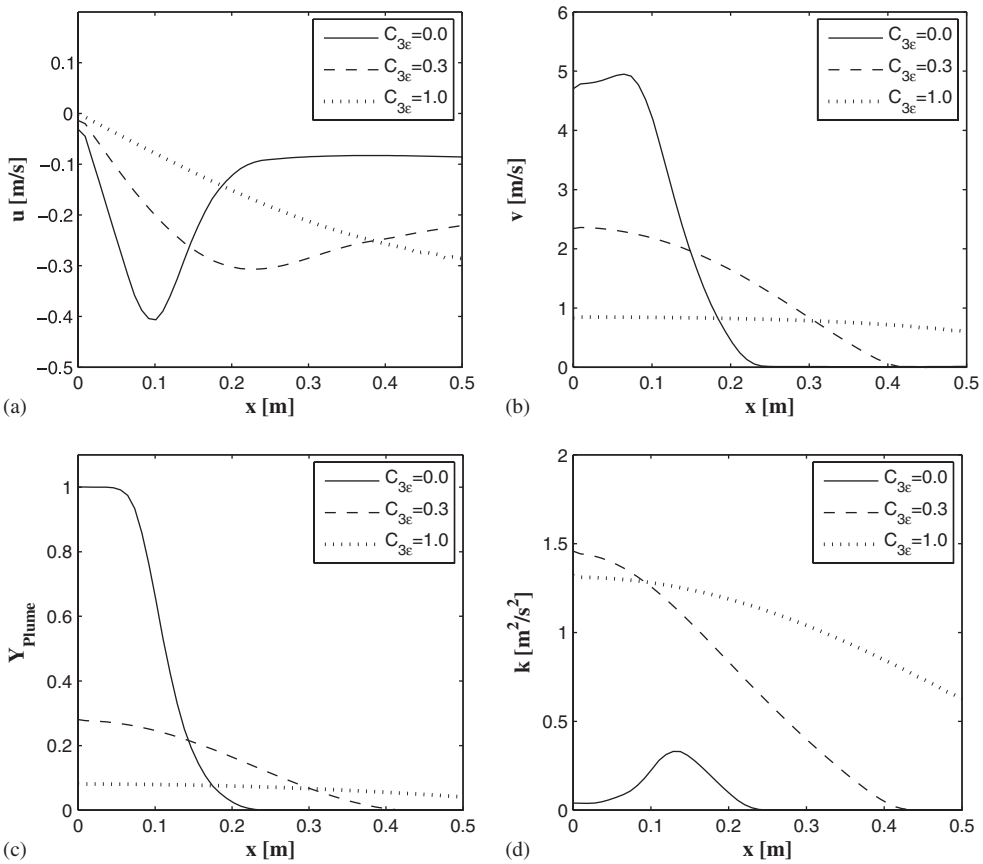

Figure 3. Effect of $C_{3\varepsilon}$ using the SGDH buoyancy model on velocity components, plume concentration and turbulent kinetic energy at $y=0.4$ m: (a) cross-stream velocity; (b) streamwise velocity; (c) plume concentration; and (d) turbulent kinetic energy.

5. RESULTS

5.1. Buoyancy-corrected-k–ε models

Results using different corrections of the standard k–ε model are now examined.

5.1.1. Effect of $C_{3\varepsilon}$. Owing to the wide range of values for $C_{3\varepsilon}$ suggested in the literature (see Tables I and II), a sensitivity analysis is performed for both buoyancy correction approaches, SGDH and GGDH. Figure 3 presents the predicted cross-stream and streamwise velocity components, the plume concentration and the turbulent kinetic energy for three values of $C_{3\varepsilon}$ $(0, 0.3$ and $1)$ for the SGDH buoyancy source term at a height of 0.4 m above the plume source. For clarity, only one axial location ($y=0.4$ m) is selected for the radial profiles, but similar trends were observed at other locations. It can be seen that $C_{3\varepsilon}$ has a great impact on the shape and magnitude of all the quantities considered. For example, the maximum streamwise velocity ranges from

DOI: 10.1002/fld

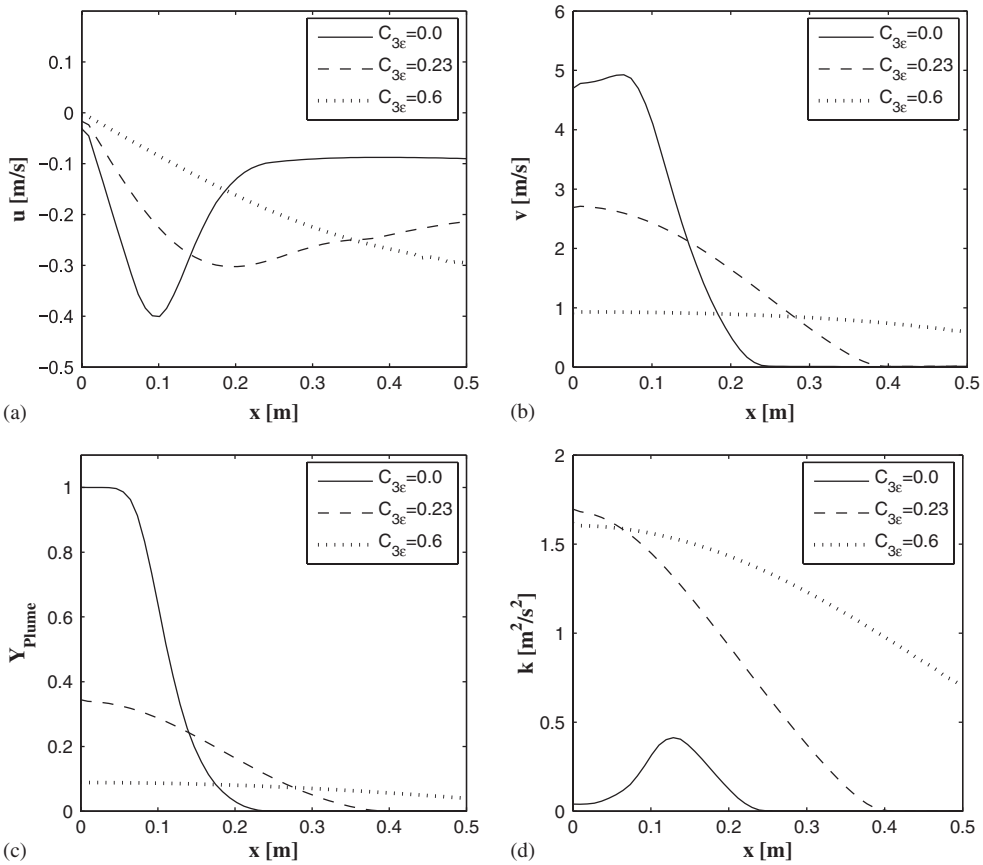

Figure 4. Effect of $C_{3\varepsilon}$ using the GGDH buoyancy model on velocity components, plume concentration and turbulent kinetic energy at $y=0.4$ m: (a) cross-stream velocity; (b) streamwise velocity; (c) plume concentration; and (d) turbulent kinetic energy.

0.85 to 4.99 m/s and the peak in the plume concentration ranges from 0.08 to 1.0. Likewise, $C_{3\varepsilon}$ is varied between 0 and 0.6 for the GGDH model and the results are shown in Figure 4. Smaller values of $C_{3\varepsilon}$ in the GGDH model have a bigger effect on the profiles compared with what is seen in Figure 3 for the SGDH model. Values of $C_{3\varepsilon}$ greater than 0.6 could not be tested due to numerical instabilities. The effects using the GGDH model are very similar to those based on the SGDH results. Further information is provided in Table IV where the peak values and spreading rates are compiled for the plume concentration, streamwise velocity and turbulent kinetic energy using the default CFX, SGDH and GGDH modified k–ε models. All three buoyancy models produce fairly similar results for the maximum values and spreading rates of the plume concentration and streamwise velocity: decreasing $C_{3\varepsilon}$ increases the spreading rate and decreases the peak value. An opposite trend for k is seen where the maximum value rises with increasing $C_{3\varepsilon}$. The present results for the near-field plume region are very different from those reported in past simulations

DOI: 10.1002/fld

Table IV. Maximum value and spreading rate comparison for the various buoyancy models.

Buoyancy model	Buoyancy constant	$Y_{\text{plume,max}}$ (dimensionless)	$r(Y_{\text{plume,max}}/2)$ (m)	$V_{\max}$ (m/s)	$r(V_{\max}/2)$ (m)	$k_{\max}$ (m^2/s^2)	$r(k_{\max}/2)$ (m)
CFX	0.00	0.10	0.45	1.02	0.53	1.12	0.44
	0.55	0.27	0.22	2.37	0.26	1.08	0.23
	1.00	1.00	0.11	4.99	0.14	0.30	0.18
SGDH	0.00	1.00	0.11	4.95	0.14	0.33	0.18
	0.30	0.28	0.22	2.36	0.26	1.46	0.22
	1.00	0.08	0.50	0.85	0.63	1.32	0.49
GGDH	0.00	1.00	0.11	4.92	0.14	0.41	0.18
	0.23	0.34	0.19	2.71	0.23	1.70	0.21
	0.60	0.09	0.47	0.93	0.58	1.62	0.46

The buoyancy constant corresponds to C_3 for the CFX model (Equation (10)) and $C_{3\varepsilon}$ for the SGDH and GGDH models (Equations (6) and (7)), $Y_{\text{plume,max}}$ is the maximum value of plume mass fraction, $r(Y_{\text{plume,max}}/2)$ the radial position where the plume concentration is equal to half its maximum value, $V_{\max}$ the maximum streamwise velocity, $r(V_{\max}/2)$ the radial position where the streamwise velocity is equal to half its maximum value, $k_{\max}$ the maximum turbulent kinetic energy and $r(k_{\max}/2)$ the radial position where the turbulent kinetic is equal to half its maximum value.

for the self-similar region of a planar helium plume [16] and thermal air plumes [9, 11, 15, 17] where no sensitivity was observed.

In this study, the sensitivity of the predictions to the buoyancy constant may be explained by the fact that the plume–air density ratio is much smaller than that in previous studies [9, 11, 15–17]. Here, the density ratio (defined as the density of the source inlet fluid divided by the density of ambient air) is equal to 0.182, which is, for example, much lower than the value for the planar plume, studied by Van Maele and Merci [16], equal to 0.75. This low density ratio is expected to be sustained in the near field of the plume where the simulation results are compared with the experimental data. This also implies that large density gradients are expected to occur in the shear layer between the inlet mixture made of 96.4% helium and ambient air. Thus, the source term G in Equations (6) and (7) will be larger in the present plume than in previous cases. Here, the density ratio is low and small changes in the value of $C_{3\varepsilon}$ in Equation (8) result in a much larger effect on $S_{\varepsilon \mathrm{B}}$.

It is also common to neglect the pressure gradient and assume that ρ_∞ is equal to $\overline{\rho}$ as used by the default CFX model in Equation (10). Near the plume inlet, it is found in the present results that the pressure gradient is in an order of magnitude less than the $\rho_\infty g_j$ and it further decreases as the flow moves away from the inlet. Thus, neglecting the pressure gradient is a reasonable approximation. However, the assumption of having ρ_∞ equal to $\overline{\rho}$ appears inaccurate in the current configuration. The source term G in CFX is much smaller by a factor of as much as 5.6 compared with the SGDH model for the same model constants.

5.1.2. SGDH and GGDH approaches. Best agreement with the experimental data is achieved for $C_{3\varepsilon}$ equal to 0.30 for the SGDH model and 0.23 for the GGDH model. For information, the best results using the CFX default model with $C_3 = 0.55$ are also shown in Figures 5 and 6. Predictions for the velocity components are displayed in Figure 5. The numerical values of the cross-stream

DOI: 10.1002/fld

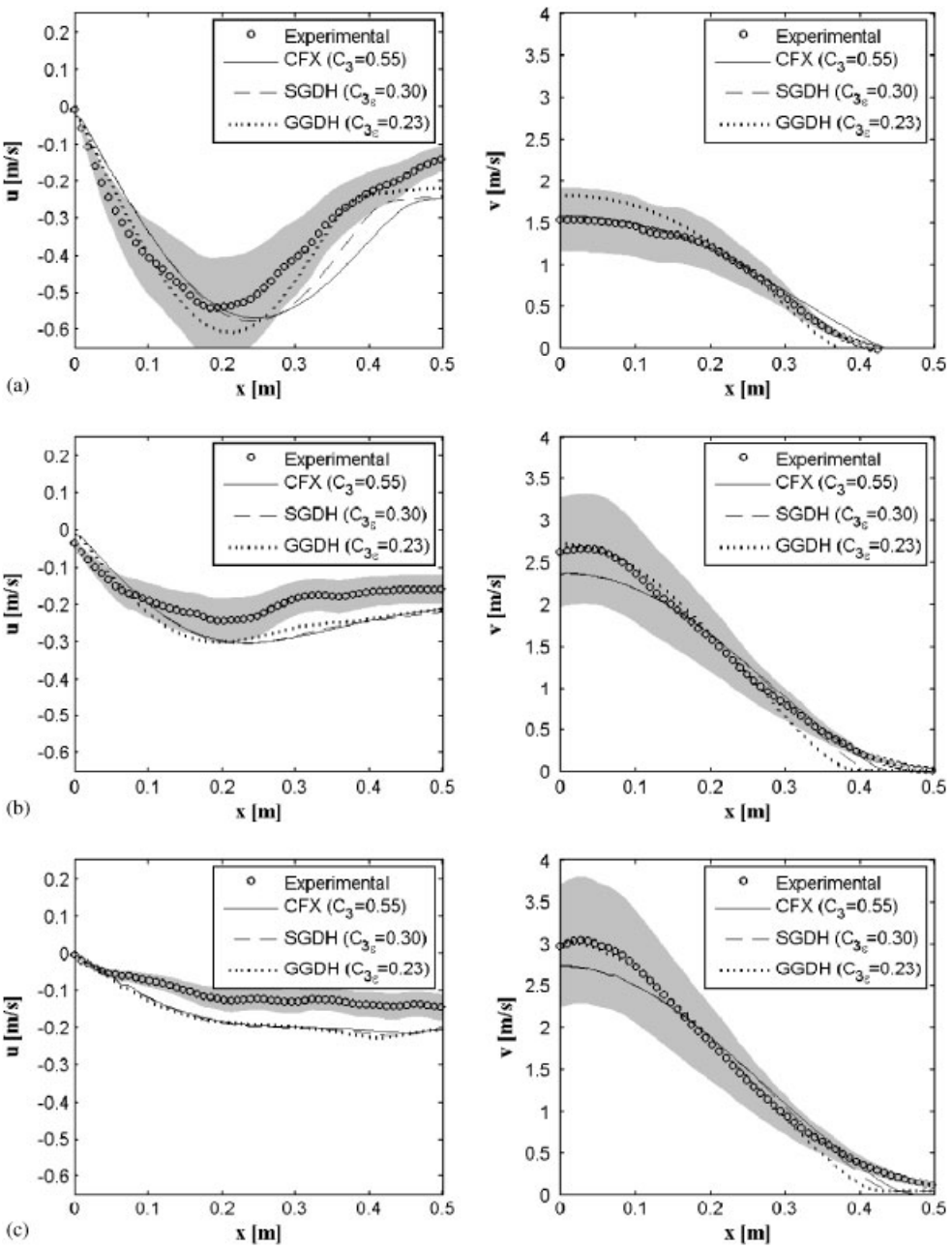

Figure 5. Comparison of the predicted cross-stream velocity (left) and streamwise velocity (right) using modified k–ε models with experimental data. The grey shaded area shows the experimental uncertainty. The same notation will be used in the subsequent figures: (a) $y=0.2\,\mathrm{m}$; (b) $y=0.4\,\mathrm{m}$; and (c) $y=0.6\,\mathrm{m}$.

DOI: 10.1002/fld

velocity follow the experimental profile for the three positions considered with the GGDH producing slightly better values. Larger differences between the predictions and the experimental values appear for positions farther downstream. The results for the streamwise velocity are in excellent agreement with the experimental data, in particular, for the SGDH model and CFX model are nearly identical producing the best match at the three axial positions considered. At $y=0.4$ and 0.6 m, the three profiles collapse together. At $y=0.2$ m, the centerline values are overpredicted by the GGDH, but at larger heights (at $y=0.4$ and 0.6 m), the differences between the simulations and the experiments are very small. Overall, the numerical values for the streamwise velocity are within the experimental uncertainties.

Figure 6 presents the radial profiles of the plume concentration and the turbulent kinetic energy compared with the experimental values. The CFX and SGDH models produce the best predictions of the plume concentration: at $y=0.2$ m, a slight underprediction is visible near the centerline and at the other locations, a small overprediction is observed. However, the profiles are wider compared with the experimental data. It is not clear why the predictions of the plume concentration are not as good as those of the streamwise velocity. Differential diffusion may be present. Inclusion of molecular diffusion did not bring any further improvement. For all models there are some discrepancies in the turbulent kinetic energy results compared with the experimental data, in particular at $y=0.2$ and 0.4 m where the numerical values are clearly larger than the experimental measurements. The additional source term G may be too large resulting in high values of k compared with the experiments. However, this overprediction does not have a significant impact on the profiles of the velocity components and plume concentration. One possible explanation is that the source term G is also found in the transport equation of the dissipation rate, ε, and higher value of G also results in higher source of dissipation in Equation (4). Consequently, the two effects may counter-act and have a smaller influence on the other quantities.

Figure 7 presents the centerline profiles of the streamwise velocity for the three models, i.e. SGDH with $C_{3\varepsilon}=0.3$, GGDH with $C_{3\varepsilon}=0.23$ and CFX with $C_3=0.55$, and the experimental values. The predictions closely follow the experimental profile and remain within the experimental uncertainty. This indicates that the transition from laminar-to-turbulent flow is well reproduced by the present numerical simulations.

A definite improvement in the results over the non-buoyant standard k–ε model [31] is found for the velocity components and plume mass fraction as long as the buoyancy constant, $C_{3\varepsilon}$, is optimized. No significant difference can be observed in the velocity components between the GGDH and SGDH models. However, the SGDH produces more accurate values for the plume concentration. No information about the transient nature of the plume such as the puffing frequency can be extracted from the RANS calculations where the transient large-scale structures are smeared out in ensemble averaging. In the following section, the capabilities of our LES are presented.

5.2. *LES*

5.2.1. Puffing frequency. When the low-density helium plume enters the enclosure, it accumulates under a layer of the higher density ambient air. The plume gas gathered until it generates a Rayleigh–Taylor instability. This is caused when a heavy fluid overlying a lighter fluid is accelerated. The lighter plume gas accelerates upward through the overlying fluid creating a toroidal vortex. The rising accelerating vortex entrains the surrounding air below it creating another heavy layer and the cycle repeats [4, 5, 22]. This phenomenon creates a puffing frequency.

DOI: 10.1002/fld

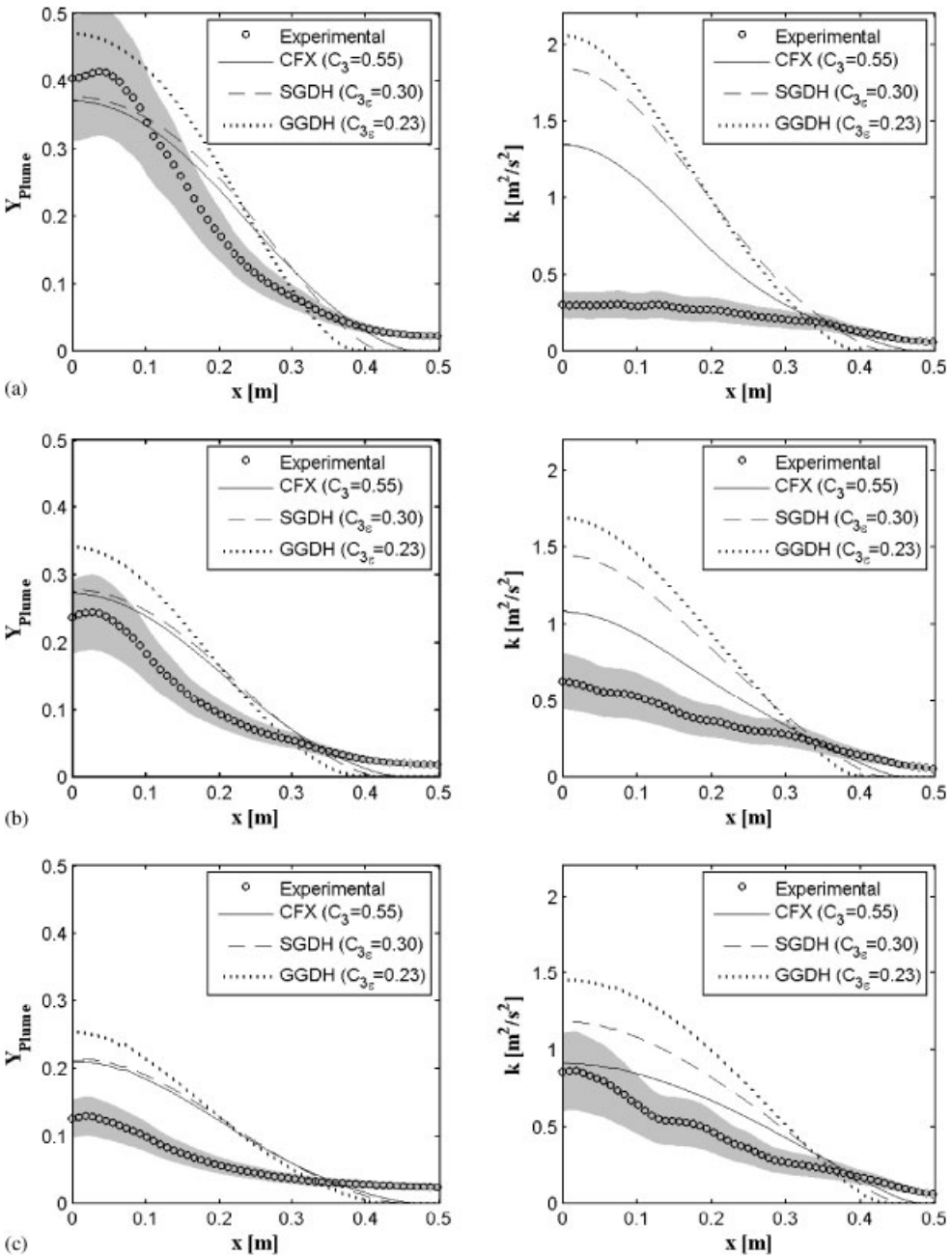

Figure 6. Comparison of the predicted plume mass fraction (left) and turbulent kinetic energy (right) using modified k–ε models with experimental data: (a) $y=0.2$ m; (b) $y=0.4$ m; and (c) $y=0.6$ m.

DOI: 10.1002/fld

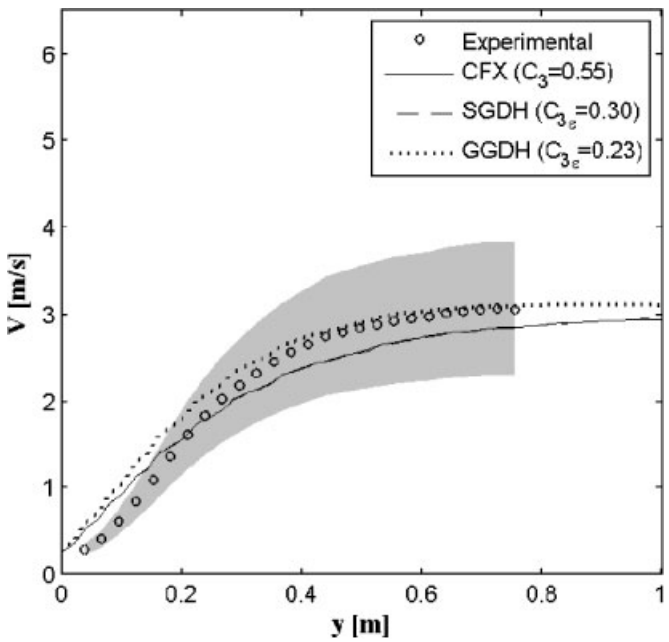

Figure 7. Centerline streamwise velocity comparison.

Figure 8 shows the time trace of streamwise velocity at a point 0.5 m above the plume source along the centerline axis. The plume puffing frequency and magnitude for the various grid sizes can be determined with the aid of these time trace plots. Puffing frequency is calculated by dividing the number of puffing cycles by the time span for these cycles. One puff cycle is characterized by a low streamwise velocity point followed by a high peak and then back to a low point. At the coarsest mesh, the puffing magnitude is very weak and the puff frequency cannot be determined. As the mesh is refined, the magnitude increases and a better estimate of the puffing frequency can be attained. Compared with the puffing frequency of the experiment of 1.36 Hz [22], the meshes of $512\times10^3, 4096\times10^3$ and 32768×10^3 cells produce puffing frequencies of 1.2, 1.3 and 1.4 Hz, respectively. As the mesh is refined, the accuracy of the puffing frequency increases and the magnitude becomes more realistic.

In the following sections, results based on the finest mesh (32768×10^3 cells) will be used. In Section 5.2.5, the effect of grid refinement will be investigated.

5.2.2. Mean flow results. The radial profiles of the time-averaged cross-stream and streamwise velocity components are displayed for six heights in Figures 9 and 10, respectively. In Figure 9 the cross-stream velocity is in reasonable agreement with the experimental values. Entrainment at the outer edges of the plume is well predicted for heights above 0.2 m. Near the centerline cross-stream velocity magnitudes are overpredicted. As shown in Figure 10, the time-averaged streamwise velocities are in good agreement with the experimental values within experimental uncertainty. As the distance from the plume source increases, the peak streamwise velocity begins to overpredict the experimental data. At $y=0.6$ m, the peak velocity moves outside the range of

DOI: 10.1002/fld

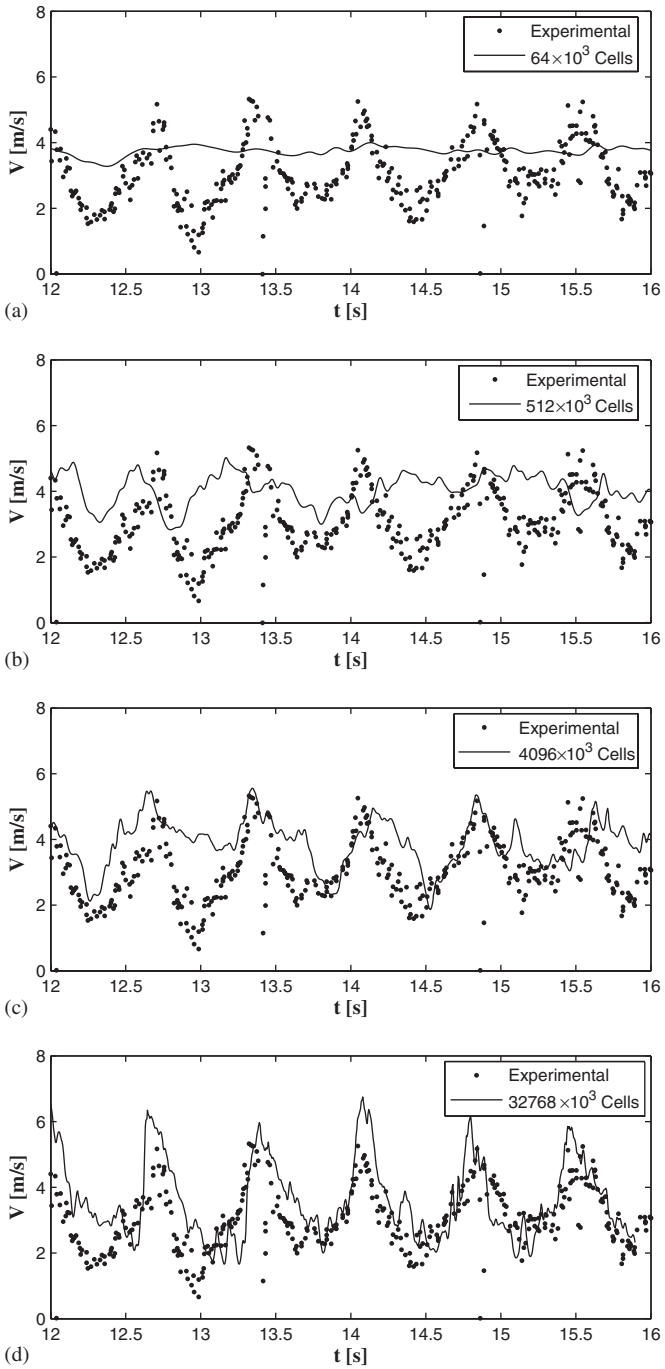

Figure 8. Time trace of streamwise velocity at $y = 0.5$ m above the plume source on the center axis for different grid resolutions: (a) 64×10^3 cells; (b) 512×10^3 cells; (c) 4096×10^3 cells; and (d) $32\,768 \times 10^3$.

DOI: 10.1002/fld

experimental uncertainty. The experimental data indicate that the streamwise velocity eventually decreases at $y \simeq 0.6$ m. This occurs farther downstream in the simulations: 1.25 m above the plume source.

Figure 11 shows the radial profiles of the plume concentration: the centerline values are higher than the experimental data and the discrepancies increase with axial distance. The predicted values are outside experimental uncertainty for axial distances above 0.3 m. To summarize, the plume concentration is well predicted at the base of the plume, but the LES results produce a much higher plume with smaller radial spreading rates compared with the experimental profiles. One possible explanation is that the buoyancy-induced turbulence from the small scales of motion is not resolved adequately with the present LES. This aspect will be investigated in Section 5.2.5. The predictions near the base of the plume where the flow is in the laminar–turbulent transition region are in good agreement with the experiments. Moving away from the plume source, the flow should get closer to a turbulent jet structure, but the rate at which it does is lower than expected. Thus, mixing rates are underpredicted and the plume rises without much lateral diffusion. The underresolved buoyancy-induced turbulence leads to the overprediction of center axis values leading to an underprediction of the mixing rates. These discrepancies may also be explained by the subgrid scale model based on a constant Smagorinsky. Desjardin *et al.* [21] observed similar trends in their results and suggested that some of the buoyancy production mechanisms occurred at the small scale and were not accounted for in the Smagorinsky model. The present results also support this conclusion. Worthy and Rubini [32] tested several subgrid scale models including the standard Smagorinsky formulation, a buoyancy-modified Smagorinsky model and different dynamic versions, applied to the turbulent buoyant plume of Shabbir and George [3]. They found that the buoyancy-corrected Smagorinsky model did not bring any further improvement compared with the standard Smagorinsky expression and that further development was needed in the dynamic models. The key for further improvement may be the inclusion of backscatter in the subgrid scale model.

5.2.3. Higher-order statistics. The radial profiles of the velocity rms are presented in Figures 12 and 13. The numerical values for both velocity rms components are well predicted and remain within the limits of experimental uncertainty at all positions, except for the outer parts of the plume. Figure 14 shows the time-averaged $u'v'$ at different heights. The shape of the experimental profiles is well predicted at all locations. At heights below 0.5 m, the predicted profiles are not as smooth as those collected in the experiments. Best agreement for the magnitude is achieved at $y = 0.5$ and 0.6 m, but there is an offset in the predictions: the peak values occur at smaller radial distances.

5.2.4. Velocity spectrum. Figure 15 shows the streamwise velocity spectrum at a height of 0.4 m along the centerline. The data was collected at a frequency of 200 Hz for the mesh of 4096×10^3 cells. The $-\frac{5}{3}$ power law of the Kolmogorov decay is shown but is not a dominant feature of the spectrum. The power spectrum decays more rapidly and a large region with a -3 power law can be noticed. This is consistent with the existence of an inertial–diffusive subrange in buoyant flows suggested by Papanicolaou [33] and evidenced in the LES simulations of Zhou *et al.* [20]. This also gives an indication that the present grid ($32\,768 \times 10^3$ cells) is fine enough to capture most of the kinetic energy produced at the large scales. Similar observations were also found for the grid consisting of 4096×10^3 cells.

DOI: 10.1002/fld

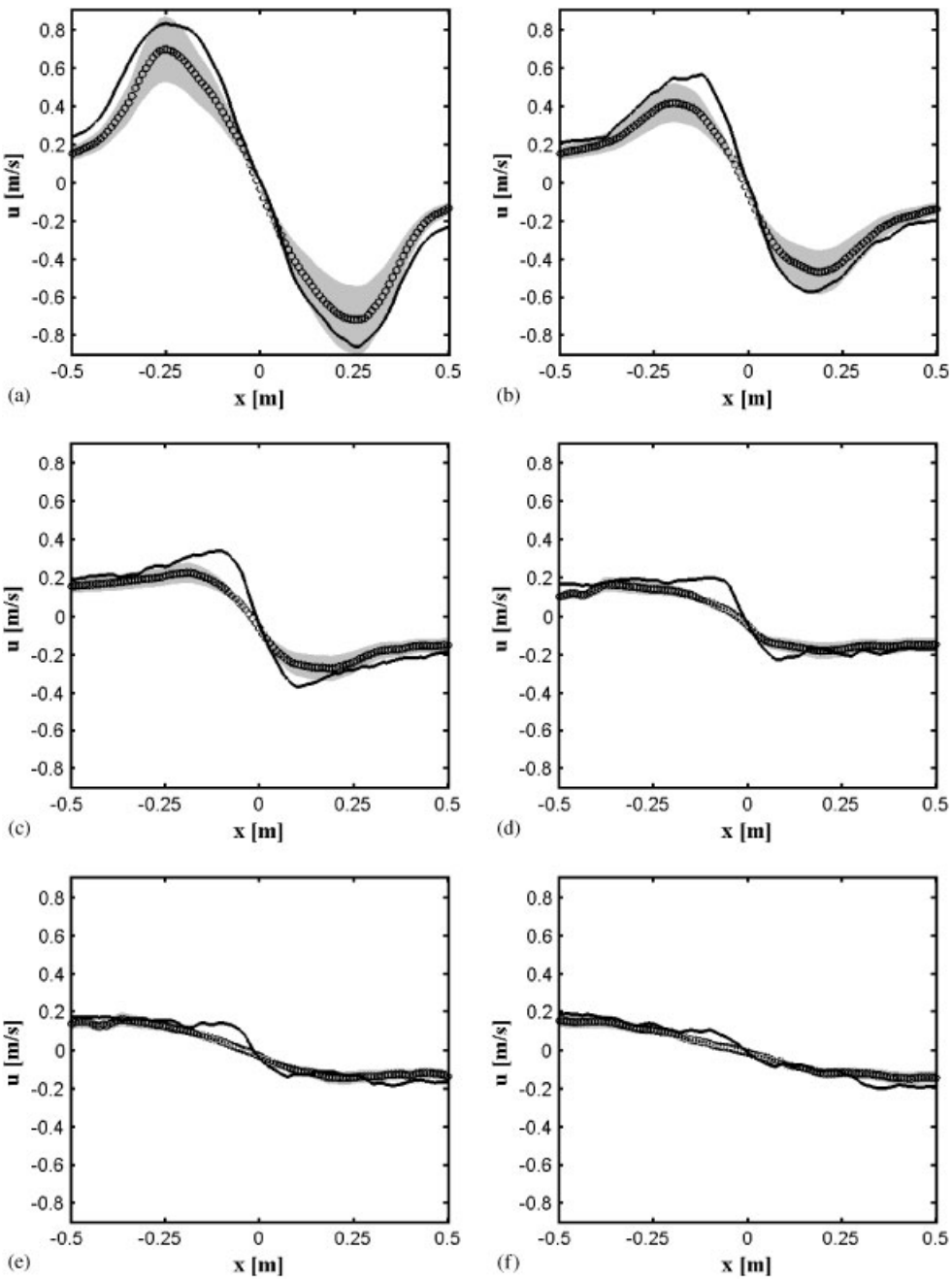

Figure 9. Comparison of time-averaged cross-stream velocity with experimental data: (a) $y=0.1\,\mathrm{m}$; (b) $y=0.2\,\mathrm{m}$; (c) $y=0.3\,\mathrm{m}$; (d) $y=0.4\,\mathrm{m}$; (e) $y=0.5\,\mathrm{m}$; and (f) $y=0.6\,\mathrm{m}$.

DOI: 10.1002/fld

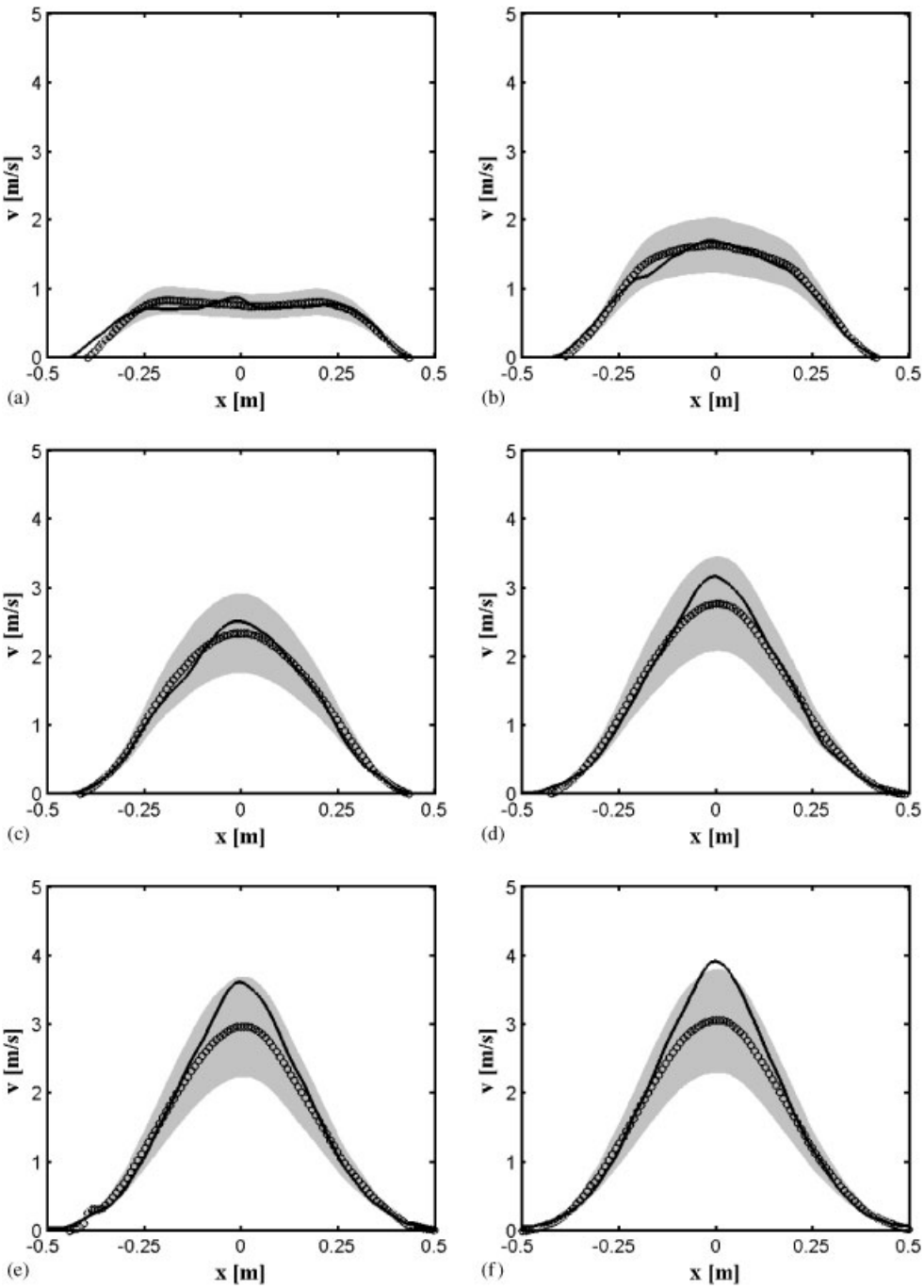

Figure 10. Comparison of time-averaged streamwise velocity with experimental data: (a) $y=0.1\,\mathrm{m}$; (b) $y=0.2\,\mathrm{m}$; (c) $y=0.3\,\mathrm{m}$; (d) $y=0.4\,\mathrm{m}$; (e) $y=0.5\,\mathrm{m}$; and (f) $y=0.6\,\mathrm{m}$.

DOI: 10.1002/fld

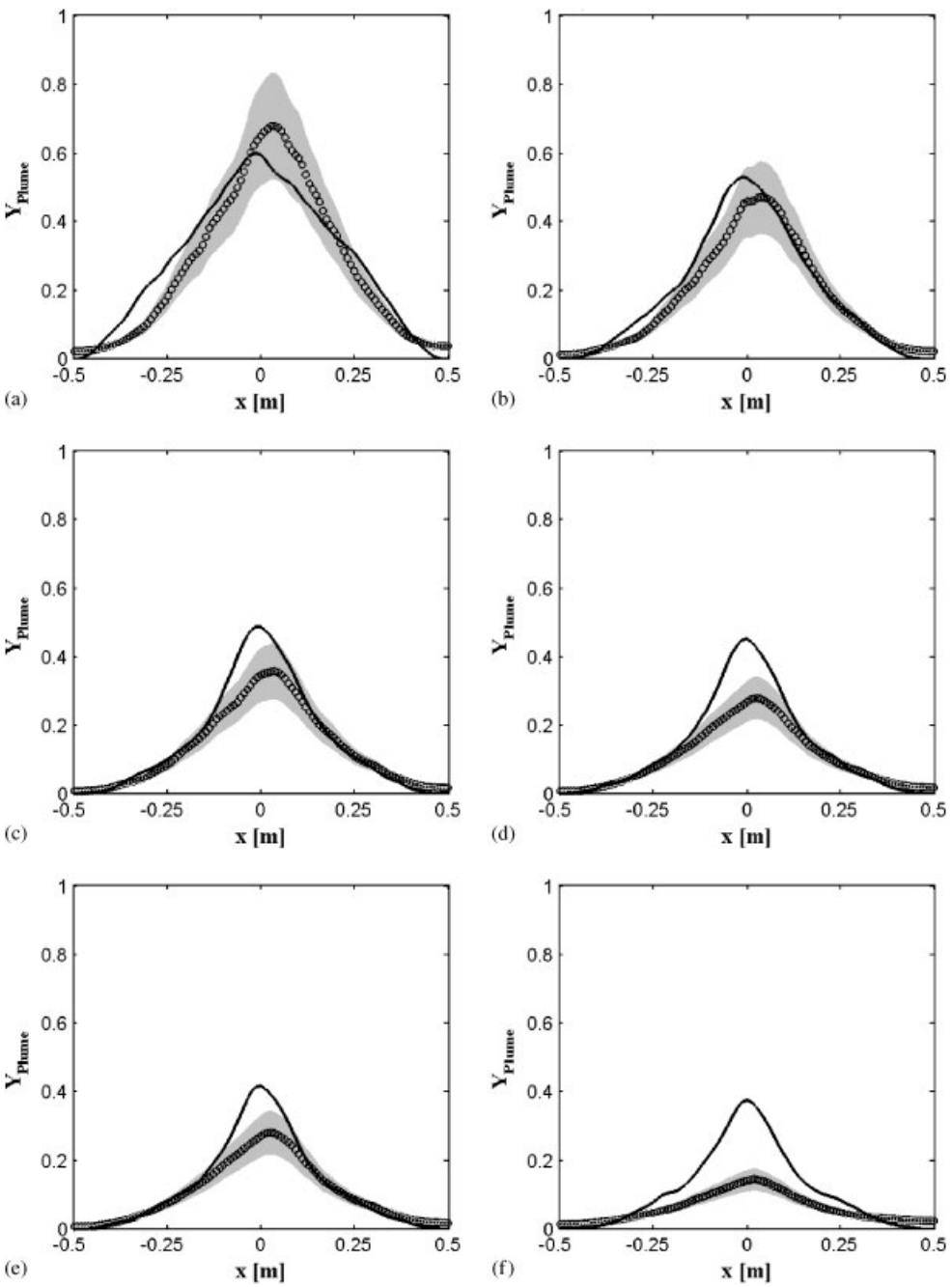

Figure 11. Comparison of time-averaged plume mass fraction with experimental data: (a) $y=0.1\,\mathrm{m}$; (b) $y=0.2\,\mathrm{m}$; (c) $y=0.3\,\mathrm{m}$; (d) $y=0.4\,\mathrm{m}$; (e) $y=0.5\,\mathrm{m}$; and (f) $y=0.6\,\mathrm{m}$.

DOI: 10.1002/fld

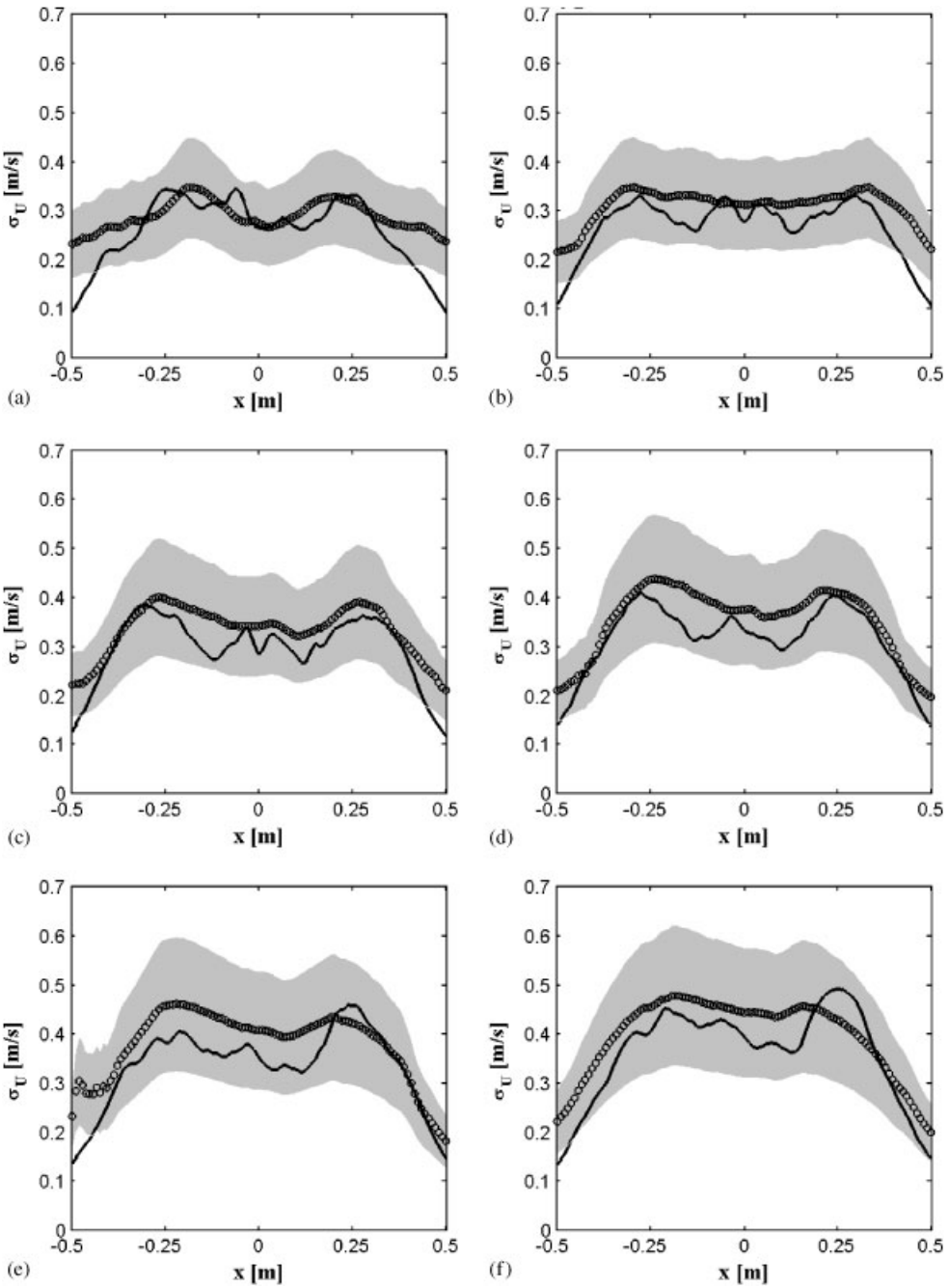

Figure 12. Comparison of the cross-stream velocity rms with experimental data: (a) $y=0.1$ m; (b) $y=0.2$ m; (c) $y=0.3$ m; (d) $y=0.4$ m; (e) $y=0.5$ m; and (f) $y=0.6$ m.

DOI: 10.1002/fld

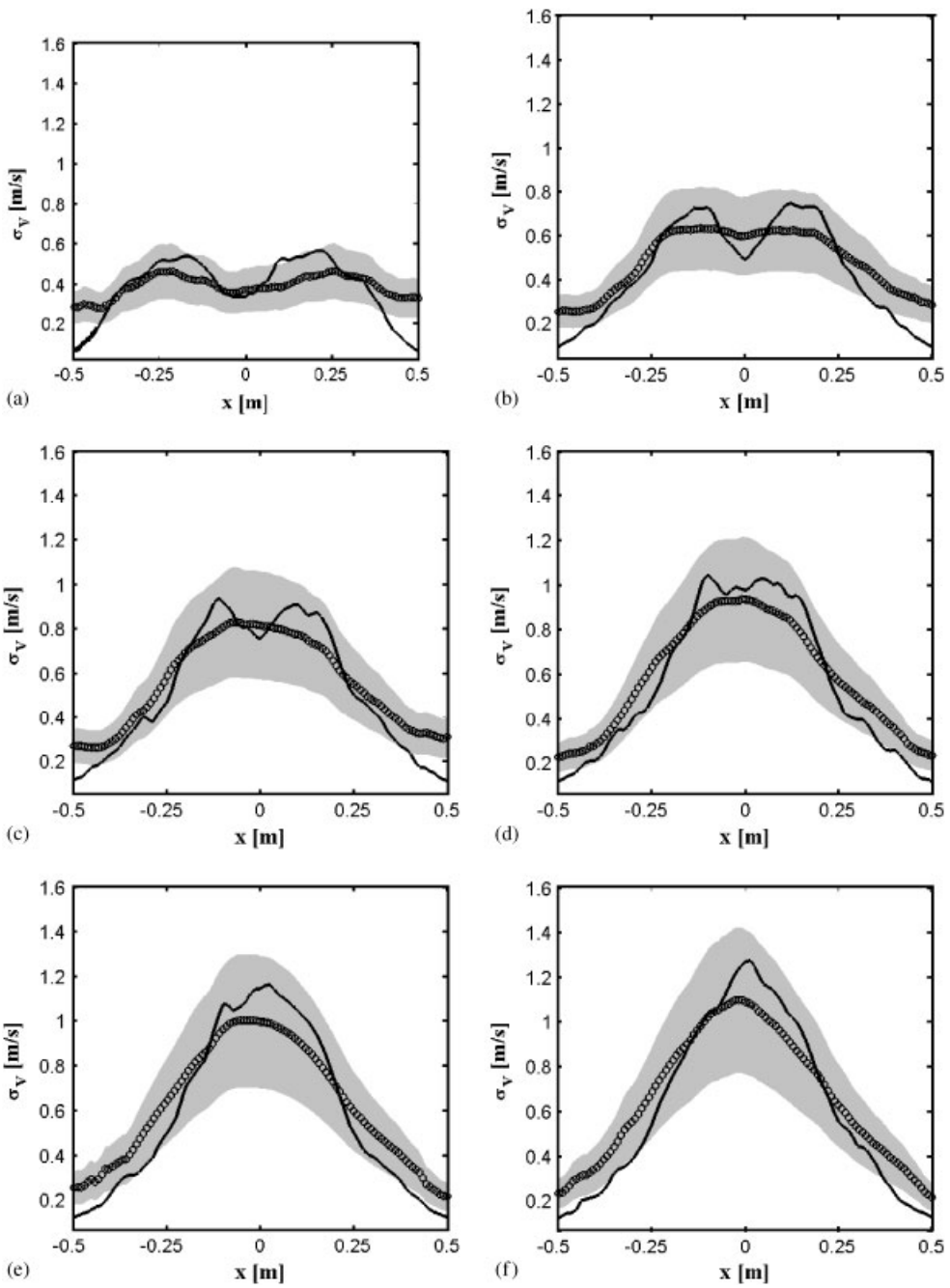

Figure 13. Comparison of the streamwise velocity rms with experimental data: (a) $y=0.1\,\mathrm{m}$; (b) $y=0.2\,\mathrm{m}$; (c) $y=0.3\,\mathrm{m}$; (d) $y=0.4\,\mathrm{m}$; (e) $y=0.5\,\mathrm{m}$; and (f) $y=0.6\,\mathrm{m}$.

DOI: 10.1002/fld

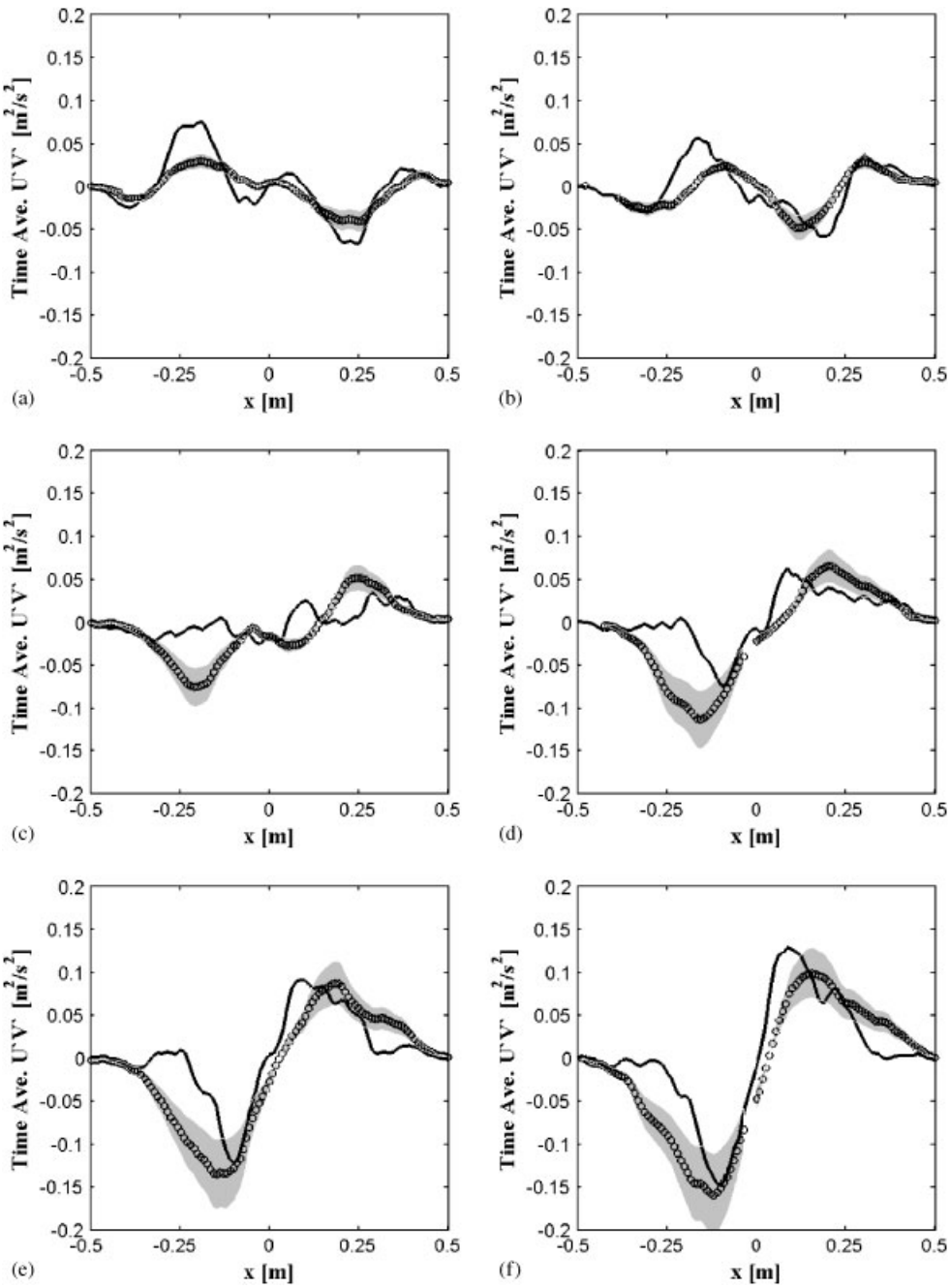

Figure 14. Comparison of the time-averaged $u'v'$ with experimental data: (a) $y=0.1\,\mathrm{m}$; (b) $y=0.2\,\mathrm{m}$; (c) $y=0.3\,\mathrm{m}$; (d) $y=0.4\,\mathrm{m}$; (e) $y=0.5\,\mathrm{m}$; and (f) $y=0.6\,\mathrm{m}$.

DOI: 10.1002/fld

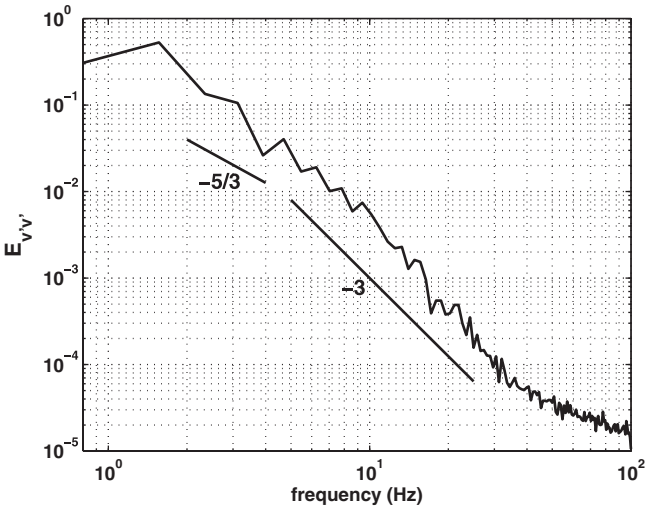

Figure 15. Power spectrum on streamwise velocity at $y=0.4\,\mathrm{m}$ along centerline.

5.2.5. Sensitivity analysis. The quality of LES calculations strongly depends on the filter width directly related to the grid resolution in the present LES code. As the grid is refined further and further, smaller and smaller eddies can be fully resolved. Thus, a trade-off must be sought between resolution required and affordable computing time. The current mesh was progressively refined and four different grids were tested: $64\times10^3, 512\times10^3, 4096\times10^3$ and $32\,768\times10^3$ cells. For clarity, only results for the last three meshes are presented in this section. Poor predictions were obtained with the coarsest mesh (64×10^3) at all positions. The mean flow statistics including the time-averaged velocity components and the plume concentration, and higher-order statistics (the velocity rms and $u'v'$) are plotted for the three grids and compared with the experimental data in Figure 16. For clarity, only one position is selected: $y=0.4\,\mathrm{m}$. However, similar trends were observed for other axial positions. As can be seen in Figure 16(a)–(c), the results for the velocity components and plume mass fraction obtained move closer to the experimental values as the grid is refined. A much more significant effect of the grid size can be noticed for the velocity rms and $u'v'$ in Figure 16(d)–(f). A finer mesh yields velocity rms and time-averaged $u'v'$ closer to the experimental data. This is consistent with what is expected to occur when smaller flow length and time scales are resolved and the impact of subgrid scale modeling is reduced.

The other important parameter in the current LES is the Smagorinsky constant C_s, which controls the amount of dissipation in the subgrid scale model. Smaller values of C_s result in lower levels of dissipation. Simulations were run for Smagorinsky constants of $0.0, 0.1, 0.2$ (default value) and 0.3 and compared with the experimental data. To save computational cost, a grid size of 4096×10^3 was used. Cross-stream velocity, streamwise velocity and plume concentration for the Smagorinsky constant values of 0.0, 0.1 and 0.2 are displayed at $y=0.4\,\mathrm{m}$ in Figure 17(a)–(c). Decreasing the Smagorinsky constant moves the numerical values closer to the experimental data for the mean flow statistics. At $y=0.4\,\mathrm{m}$, best agreement with the experimental data is achieved for $C_s=0$ (corresponding to no subgrid scale model): the numerical values are within

DOI: 10.1002/fld

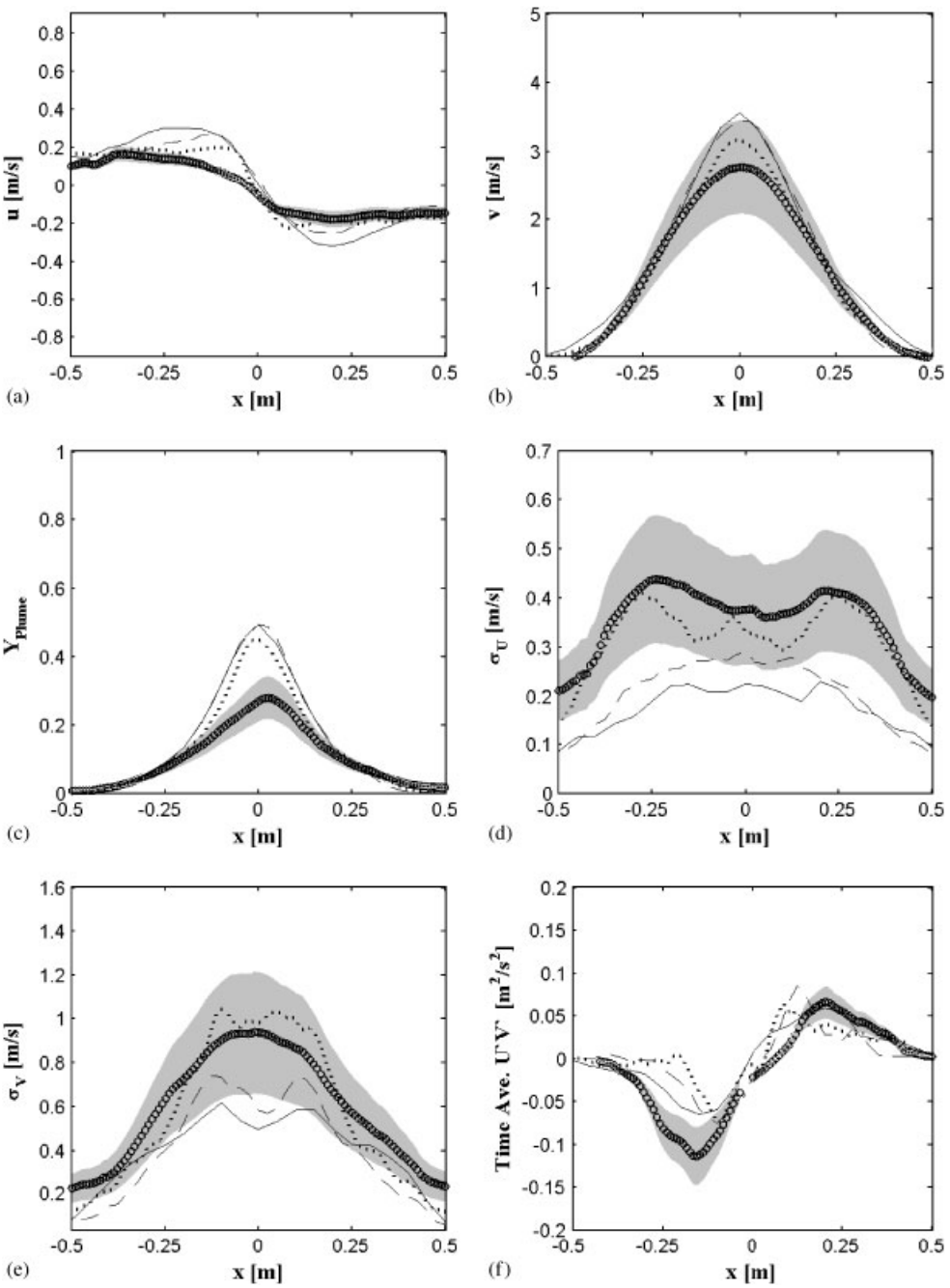

Figure 16. Effect of the grid size at $y = 0.4\,\mathrm{m}$ (○ experimental, — 512×10^3, - - 4096×10^3, $\cdots$ $32\,768 \times 10^3$): (a) cross-stream velocity; (b) streamwise velocity; (c) plume mass fraction; (d) cross-stream velocity rms; (e) streamwise velocity rms; and (f) $u'v'$.

DOI: 10.1002/fld

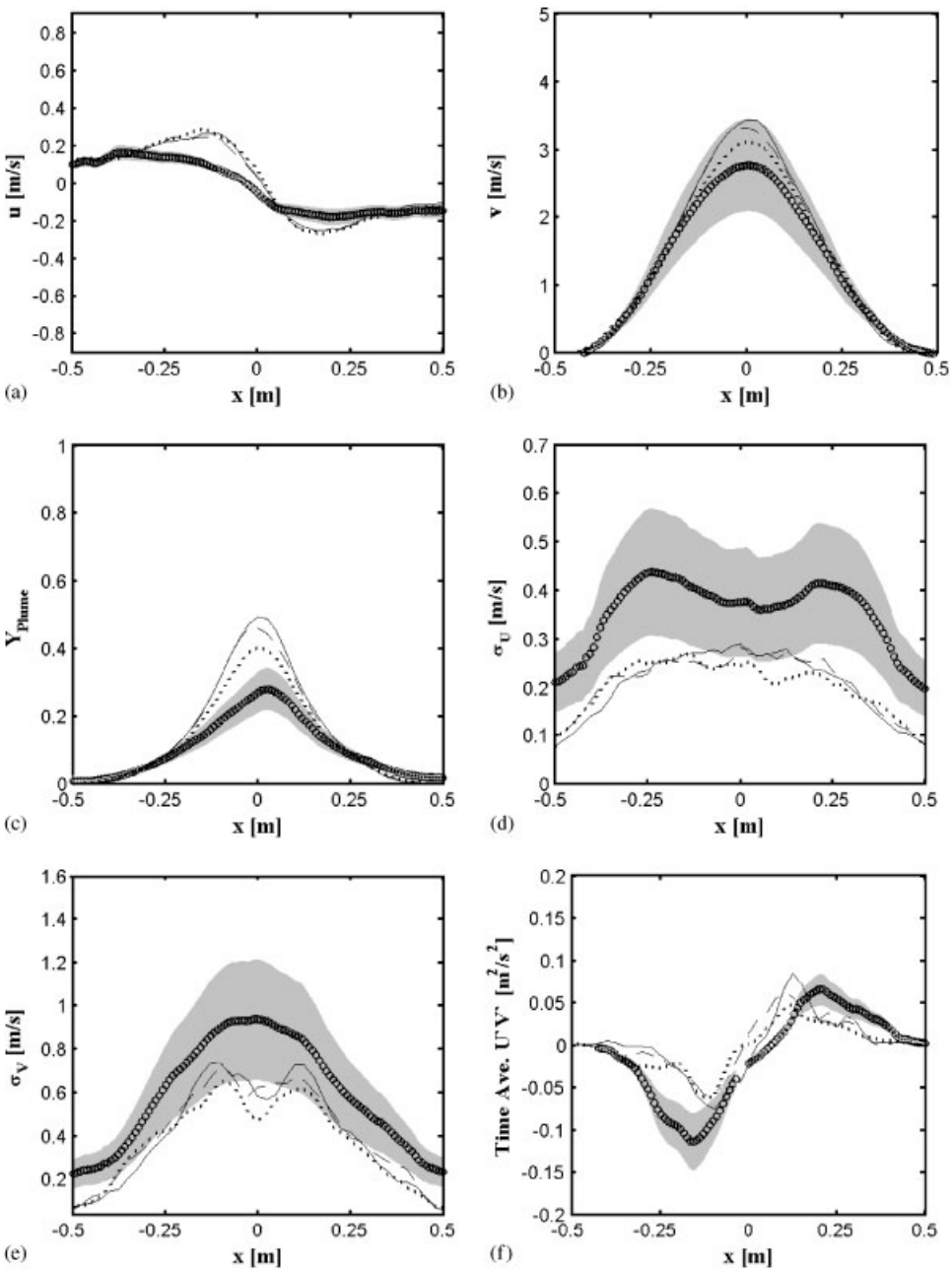

Figure 17. Effect of the Smagorinsky constant on the time-averaged cross-stream velocity, streamwise velocity, plume concentration, cross-stream velocity rms, streamwise velocity rms and $u'v'$ for the mesh of 4096×10^3 cells at $y = 0.4$ m ($\circ$ experimental, — $C_s = 0.0$, - - $C_s = 0.1, \cdots C_s = 0.2$): (a) cross-stream velocity; (b) streamwise velocity; (c) plume mass fraction; (d) cross-stream velocity rms; (e) streamwise velocity rms; and (f) $u'v'$.

DOI: 10.1002/fld

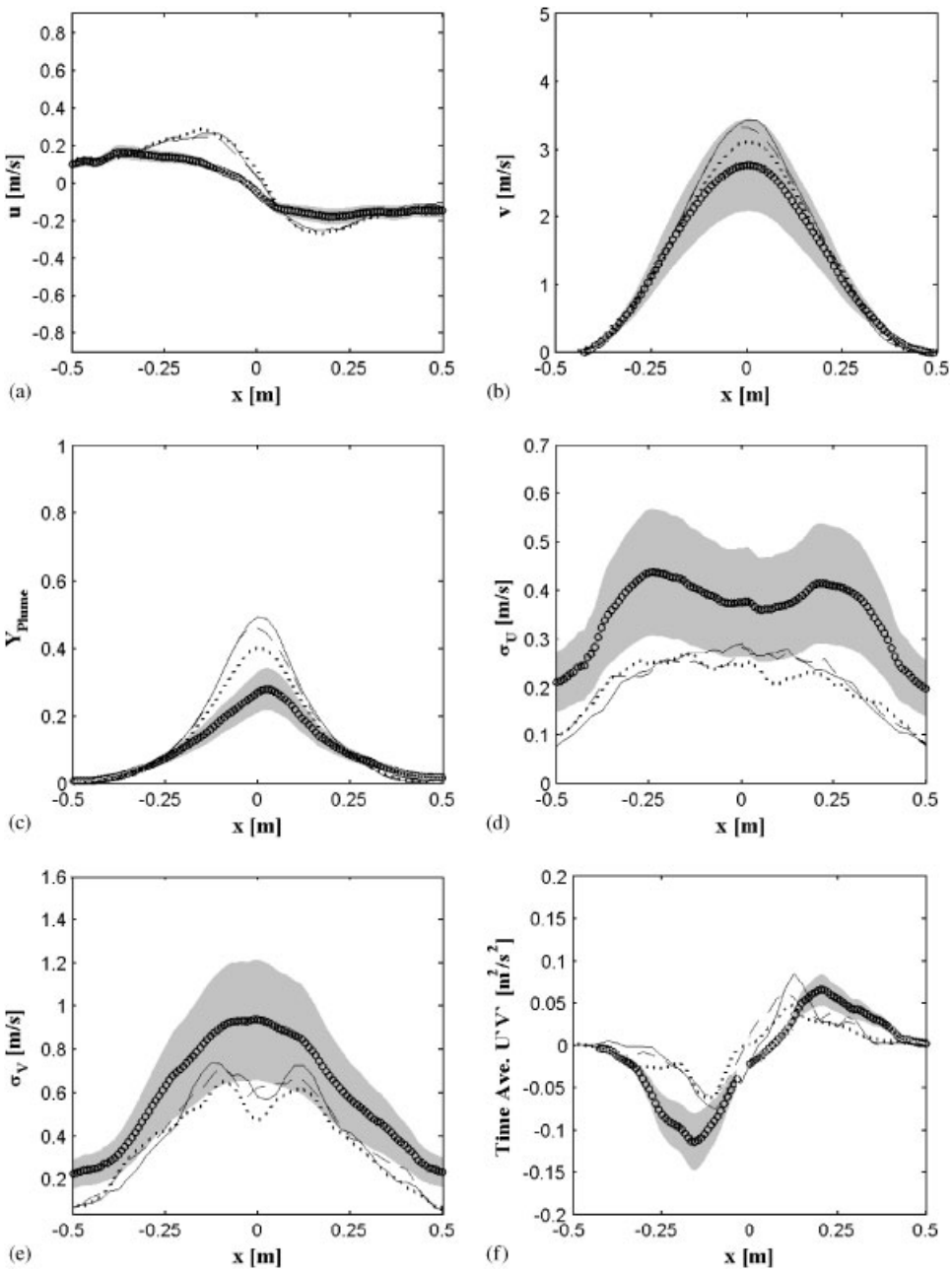

Figure 18. Effect of the Schmidt number on the time-averaged cross-stream velocity, streamwise velocity, plume concentration, cross-stream velocity rms, streamwise velocity rms and $u'v'$ for the mesh of 4096×10^3 cells at $y = 0.4$ m ($\circ$ experimental, — $Sc = 0.5$, - - $Sc = 0.6$, $\cdots Sc = 1.0$): (a) cross-stream velocity; (b) streamwise velocity; (c) plume mass fraction; (d) cross-stream velocity rms; (e) streamwise velocity rms; and (f) $u'v'$.

DOI: 10.1002/fld

the experimental uncertainty. However, it should be noted that near the plume source ($y \leqslant 0.3\,\mathrm{m}$), the results for the plume concentration using $C_s = 0$ significantly underpredict the experimental data and are outside the experimental uncertainty region. In this region better predictions are obtained for C_s equal to 0.1. Some possible improvement on the mean flow statistics may be reached by decreasing the Smagorinsky constant, but this needs to be balanced with the significant impact of C_s on the fluctuating properties, as shown in Figure 17(d)–(f). Decreasing C_s moves the cross-stream velocity closer to the experimental profiles. However, an opposite trend is observed for the streamwise velocity rms shown in Figure 17(e) where best agreement is obtained for $C_s = 0.2$. The influence of C_s on the time-averaged $u'v'$ is small. It is difficult to determine the general effect of C_s on the predictions. The magnitude of the impact and the trends are different according to the quantity considered. Furthermore, the effect of C_s will also depend on the mesh resolution. The value of C_s becomes less significant as the mesh is refined. Thus, C_s must be changed with caution and it seems to be best to keep a value between 0.15 and 0.2 for the present grid.

The last parameter that may affect the results is the Schmidt number in Equation (12). Figure 18 shows the results for the velocity components, the plume concentration, the velocity rms and the time-averaged $u'v'$ at $y = 0.4\,\mathrm{m}$ for three values of Sc (0.5, 0.6 and 1). As can be seen, the turbulent Schmidt has a very small effect on the predictions. The biggest relative impact is on the streamwise and plume concentration profiles. The small effect of the Schmidt number indicates that the transport mechanisms at the resolved scale are advection dominated. This was also observed in previous LES calculations [28, 34].

6. CONCLUSIONS

In RANS, the addition of buoyancy source terms via the SGDH and GGDH model resulted in excellent agreement with the experimental data for both the streamwise velocity and plume concentration profiles as long as an optimized buoyancy constant value can be found. Differences between the prediction using the SGDH approach and those using the GGDH model were small. Overall, the SGDH model demonstrated the best performance in plume concentration, whereas the GGDH model produced the best results for the streamwise velocity. However, these results were shown to be sensitive to the buoyancy constant $C_{3\varepsilon}$. This is a serious drawback for the present RANS simulations and it is expected that the constant may have to be tuned depending on the conditions of the buoyant plume to be modeled. Further improvement may be brought by implementing a second-moment closure to model the Reynolds stresses [35].

The LES results were in very good agreement with the experimental data. The predicted puffing frequency was very close to the experimental value and the instantaneous contours were consistent with the experimental observations. The velocity plots indicated that the numerical results were predicted within the limits of experimental uncertainty, while the plume concentration contours showed that the present LES results overpredicted the experimental data near the centerline. Some sensitivity of the results to the mesh was observed. Best agreement was achieved with the finest mesh tested, i.e. $32\,768 \times 10^3$ cells but a good compromise for the mesh size in terms of accuracy of the predictions and CPU time may be the 4096×10^3-cell-mesh. Further grid refinement produced better time-averaged velocity components and plume concentration. The fluctuating quantities are much more sensitive to the grid size. It was shown that the

DOI: 10.1002/fld

Smagorinsky constant had a large impact on the predictions. Unless a dynamic model is used, a value between 0.15 and 0.2 gave the best overall results. Very little sensitivity was noticed for the Schmidt number. A subgrid scale model where the backscatter is allowed may yield further improvement [36].

The choice of the most suitable method strongly depends on the expected level of accuracy, computational resources and available timeframe. Future development may rely on hybrid RANS-LES techniques where the transient large-scale structures are resolved using LES and advanced RANS models are included [35].

NOMENCLATURE

$C_{1\varepsilon}$	model constant in turbulent dissipation equation
$C_{2\varepsilon}$	model constant in turbulent dissipation equation
C_3	CFX buoyancy constant
$C_{3\varepsilon}$	buoyancy constant
C_s	Smagorinsky constant
C_μ	turbulent viscosity constant
D_{sgs}	subgrid diffusivity (m^2/s)
G	production of turbulent kinetic energy due to buoyancy ($kg/m\,s^3$)
P	production of turbulent kinetic energy due to shear ($kg/m\,s^3$)
R_f	flux Richardson number
Ri	Richardson number
Re	Reynolds number
S	filtered rate of strain ($1/s$)
S_ε	dissipation equation source term ($kg/m\,s^4$)
$S_{\varepsilon B}$	effect of buoyancy source term in the turbulent dissipation equation ($kg/m\,s^4$)
$\tilde{S}_{ij}$	strain tensor ($1/s$)
Sc	Schmidt number
g_j	gravitational acceleration (m/s^2)
k	turbulent kinetic energy (m^2/s^2)
p	pressure (N/m^2)
t	time (s)
u_i	velocity component in the i-direction (m/s)
x_i	coordinate direction (m)
u	cross-stream velocity (m/s)
v	streamwise velocity (m/s)
Y_{plume}	plume mass fraction (dimensionless)
Δ	filter width (m)
Δ_i	grid spacing in the i-direction (m)
δ_{ij}	Kronecker delta
ε	rate of dissipation of turbulent kinetic energy (m^2/s^3)

DOI: 10.1002/fld

μ	molecular viscosity (kg/m s)
μ_t	turbulent or eddy viscosity (kg/m s)
μ_{sgs}	subgrid viscosity (kg/m s)
ρ	density (kg/m^3)
ρ_0	source gas density (kg/m^3)
ρ_∞	reference density (kg/m^3)
σ_k	turbulent Prandtl number for kinetic energy
σ_t	turbulent Prandtl number for production of turbulent kinetic energy due to buoyancy
σ_ε	turbulent Prandtl number for dissipation
σ_ρ	CFX model constant
σ_u	cross-stream velocity rms in LES
σ_v	streamwise velocity rms in LES
$\overline{\phi}$	Reynolds-averaged quantity (RANS)
ϕ'	fluctuating component (Reynolds statistic)
ϕ''	fluctuating component (Favre statistic)

ACKNOWLEDGEMENTS

Financial support from NSERC is gratefully acknowledged.

REFERENCES

1. Tieszen SR. On the fluid mechanics of fires. *Annual Review of Fluid Mechanics* 2001; **33**:67–92.
2. Heskestad G. Dynamics of the fire plume. *Philosophical Transactions of the Royal Society of London Series A* 1998; **356**:2815–2833.
3. Shabbir A, George WK. Experiments on a round turbulent buoyant plume. *Journal of Fluid Mechanics* 1994; **275**:1–32.
4. Cetegen BM, Ahmed TA. Experiments on the periodic instability of buoyant plumes and pool fires. *Combustion and Flame* 1993; **93**:157–184.
5. Cetegen BM, Kasper KD. Experiments on the oscillatory behaviour of buoyant plumes of helium and helium–air mixtures. *Physics of Fluids* 1996; **8**:2974–2984.
6. Yuan T, Durox D, Villermaux E. An analogue study for flame flickering. *Experiments in Fluids* 1994; **17**:337–349.
7. Lingens A, Reeker M, Schriber M. Instability of buoyant diffusion flames. *Experiments in Fluids* 1996; **20**: 241–248.
8. Davidson L. Second-order corrections of the k–ε model to account for non-isotropic effects due to buoyancy. *International Journal of Heat and Mass Transfer* 1990; **33**:2599–2608.
9. Shabbir A, Taulbee DB. Evaluation of turbulence models for predicting buoyant flows. *Journal of Heat Transfer* 1990; **112**:945–951.
10. Chow WK, Mok WK. CFD fire simulations with four turbulence models and their combinations. *Journal of Fire Sciences* 1999; **17**:209–231.
11. Markatos NC, Malin MR. Mathematical modeling of buoyancy-induced smoke flow in enclosures. *International Journal of Heat and Mass Transfer* 1982; **25**:63–75.
12. Daly BJ, Harlow FH. Transport equations in turbulence. *Physics of Fluids* 1970; **13**:2634–2649.
13. Nam S, Bill Jr RG. Numerical simulation of thermal plumes. *Fire Safety Journal* 1993; **21**:231–256.
14. Yan Z, Holmstedt G. A two-equation turbulence models and its application to a buoyant diffusion flame. *International Journal of Heat and Mass Transfer* 2001; **42**:1305–1315.
15. Worthy J, Sanderson V, Rubini P. Comparison of modified k–ε turbulence models for buoyant plumes. *Numerical Heat Transfer* 2001; **39**:151–165.

DOI: 10.1002/fld

16. Van Maele K, Merci B. Application of two buoyancy-modified k–ε turbulence models to different types of buoyant plumes. *Fire Safety Journal* 2006; **41**:122–318.
17. Brescianini CP, Delichatsios MA. New evaluation of the k–ε turbulence model for free buoyant plumes. *Numerical Heat Transfer* 2003; **43**:731–751.
18. Annarumma MO, Most JM, Joulain P. On the numerical modeling of buoyancy-dominated turbulent vertical diffusion flames. *Combustion and Flame* 1991; **85**:403–415.
19. Xue H, Ho JC, Cheng YM. Comparison of different combustion models in enclosure fire simulation. *Fire Safety Journal* 2001; **36**:37–54.
20. Zhou X, Luo KH, Williams JJR. Study of density effects in turbulent buoyant jets using large eddy simulation. *Theoretical and Computational Fluid Dynamics* 2001; **15**:95–120.
21. Desjardin PE, O'Hern TJ, Tieszen SR. Large eddy simulation and experimental measurements of the near-field of a large turbulent helium plume. *Physics of Fluids* 2004; **16**:1866–1883.
22. O'Hern TJ, Weckman EJ, Gerhart AL, Tieszen SR, Schefer RW. Experimental study of a turbulent buoyant helium plume. *Journal of Fluid Mechanics* 2005; **544**:143–171.
23. Jones WP, Launder BE. The prediction of laminarization with a two-equation model of turbulence. *International Journal of Heat and Mass Transfer* 1972; **15**:301–314.
24. Ohira N, Murakami S, Kato S. CFD analysis of a thermal plume and the indoor air flow using k–ε models with buoyancy effects. *Flow*, *Turbulence and Combustion* 1999; **63**:113–134.
25. Rodi W. Turbulence models and their application in hydraulics. *Ph.D. Thesis*, University of Karlsruhe, 1980.
26. Ansys. *CFX 10.0 Technical Reference Guide*, 2005.
27. McGrattan KB, Baum HR, Rehm RG. Numerical simulation of smoke plumes from large oil fires. *Atmospheric Environment* 1996; **30**:4125–4136.
28. Xin Y, Gore J, McGrattan KB, Rehm RG, Baum HR. Large eddy simulation of buoyant turbulent pool fires. *Proceedings of the Combustion Institute* 2002; **29**:259–266.
29. Smagorinsky J. General circulation experiments with the primitive equations. I. The basic experiment. *Monthly Weather Review* 1963; **91**:99–164.
30. Sandia National Laboratories. http://192.84.24.155/datasite_viv.cfm.
31. Chung W, Devaud CB. Buoyancy-corrected k–ε turbulence models and large eddy simulation applied to a helium plume. *Proceedings*, University of Toronto, Canada, Canadian Society of CFD, May 2007; 1–6.
32. Worthy JAG, Rubini PA. A study of LES stress and flux models applied to a buoyant jet. *Numerical Heat Transfer Part B* 2005; **48**:235–256.
33. Papanicolaou PN, List EJ. Investigations of round turbulent buoyant jets. *Journal of Fluid Mechanics* 1988; **195**:341–491.
34. Zhang W, Hamer A, Klassen M, Carpenter D, Roby R. Turbulent statistics in a fire room model by large eddy simulation. *Fire Safety Journal* 2002; **37**:721–752.
35. Hanjalic K. One-point closure models for buoyancy-driven turbulent flows. *Annual Review of Fluid Mechanics* 2002; **34**:321–347.
36. Brown AR, Derbyshire SH, Mason PJ. Large-eddy simulation of stable atmospheric boundary layers with a revised stochastic subgrid model. *Quarterly Journal of the Royal Meteorological Society* 1994; **120**:1485–1512.

DOI: 10.1002/fld